Observation of inverse Compton emission from a long γ-ray burst

Inverse Compton emission revealed by multi-wavelength observations of a gamma-ray burst

The MAGIC Collaboration: V. A. Acciari[1], S. Ansoldi[2,21], L. A. Antonelli[3], A. Arbet Engels[4], D. Baack[5], A. Babić[6], B. Banerjee[7], U. Barres de Almeida[8], J. A. Barrio[9], J. Becerra González[1], W. Bednarek[10], L. Bellizzi[11], E. Bernardini[12,16], A. Berti[13,25], J. Besenrieder[14], W. Bhattacharyya[12], C. Bigongiari[3], A. Biland[4], O. Blanch[15], G. Bonnoli[11], Ž. Bošnjak[6], G. Busetto[16], R. Carosi[17], G. Ceribella[14], Y. Chai[14], A. Chilingaryan[22], S. Cikota[6], S. M. Colak[15], U. Colin[14], E. Colombo[1], J. L. Contreras[9], J. Cortina[27], S. Covino[3], V. D'Elia[3], P. Da Vela[17], F. Dazzi[3], A. De Angelis[16], B. De Lotto[2], M. Delfino[15,26], J. Delgado[15,26], D. Depaoli[13], F. Di Pierro[13], L. Di Venere[13], E. Do Souto Espiñeira[15], D. Dominis Prester[6], A. Donini[2], D. Dorner[18], M. Doro[16], D. Elsaesser[5], V. Fallah Ramazani[19], A. Fattorini[5], A. Fernández-Barral[16], G. Ferrara[3], D. Fidalgo[9], L. Foffano[16], M. V. Fonseca[9], L. Font[20], C. Fruck[14], S. Fukami[21], S. Gallozzi[3], R. J. García López[1], M. Garczarczyk[12], S. Gasparyan[22], M. Gaug[20], N. Giglietto[13], F. Giordano[13], N. Godinović[6], D. Green[14], D. Guberman[15], D. Hadasch[21], A. Hahn[14], J. Herrera[1], J. Hoang[9], D. Hrupec[6], M. Hütten[14], T. Inada[21], S. Inoue[21], K. Ishio[14], Y. Iwamura[21], L. Jouvin[15], D. Kerszberg[15], H. Kubo[21], J. Kushida[21], A. Lamastra[3], D. Lelas[6], F. Leone[3], E. Lindfors[19], S. Lombardi[3], F. Longo[2,25], M. López[9], R. López-Coto[16], A. López-Oramas[1], C. Maggio[20], P. Majumdar[7], M. Makariev[23], M. Mallamaci[16], G. Maneva[23], M. Manganaro[6], K. Mannheim[18], L. Maraschi[3], M. Mariotti[16], M. Martínez[15], S. Masuda[21], D. Mazin[14,21], S. Mićanović[6], D. Miceli[2], M. Minev[23], J. M. Miranda[11], R. Mirzoyan[14], E. Molina[24], A. Moralejo[15], D. Morcuende[9], V. Moreno[20], E. Moretti[15], P. Munar-Adrover[20], V. Neustroev[19], C. Nigro[12],

K. Nilsson[19], D. Ninci[15], K. Nishijima[21], K. Noda[21], L. Nogués[15], M. Nöthe[5], S. Nozaki[21], S. Paiano[16], J. Palacio[15], M. Palatiello[2], D. Paneque[14], R. Paoletti[11], J. M. Paredes[24], P. Peñil[9], M. Peresano[2], M. Persic[2], P. G. Prada Moroni[17], E. Prandini[16], I. Puljak[6], W. Rhode[5], M. Ribó[24], J. Rico[15], C. Righi[3], A. Rugliancich[17], L. Saha[9], N. Sahakyan[22], T. Saito[21], S. Sakurai[21], K. Satalecka[12], K. Schmidt[5], T. Schweizer[14], J. Sitarek[10], I. Šnidarić[6], D. Sobczynska[10], A. Somero[1], A. Stamerra[3], D. Strom[14], M. Strzys[14], Y. Suda[14], T. Surić[6], M. Takahashi[21], F. Tavecchio[3], P. Temnikov[23], T. Terzić[6], M. Teshima[14,21], N. Torres-Albà[24], S. Tsujimoto[21], J. van Scherpenberg[14], G. Vanzo[1], M. Vazquez Acosta[1], C. F. Vigorito[13], I. Vovk[14], M. Will[14], D. Zarić[6] & L. Nava[2,3],

For the Fermi Gamma-ray Burst (GBM) team:

P. Veres[40], P. N. Bhat[40], M. S. Briggs[40,41], W. H. Cleveland[39], R. Hamburg[40,41], C. M. Hui[35], B. Mailyan[40], R. D. Preece[40,41], O. Roberts[39], A. von Kienlin[42], C. A. Wilson-Hodge[35],

For the Fermi Large Area Telescope (LAT) collaboration:

D. Kocevski[35], M. Arimoto[28], D. Tak[76,102], K. Asano[29], M. Axelsson[30,31], G. Barbiellini[2,25], E. Bissaldi[32,33], R. Gill[34], J. Granot[34], J. McEnery[76,102], N. Omodei[36], F. Piron[37], J. L. Racusin[102], S. Razzaque[38], M. N. Takahashi[14], D. J. Thompson[102],

For the Swift collaboration:

S. Campana[43], M. G. Bernardini[43], N. P. M. Kuin[44], M. H. Siegel[45], S. Bradley Cenko[102,46], P.

OBrien[62], A. DAì[47], M. De Pasquale[48], J. Gropp[45], N. Klingler[45], J. P. Osborne[62], M. Perri[53,52], R. Starling[62], G. Tagliaferri[43,47], A. Tohuvavohu[45],

For the AGILE collaboration:

A. Ursi[49], M. Tavani[49,50,51], M. Cardillo [49], C. Casentini [49], G. Piano[49], Y. Evangelista[49], F. Verrecchia[52,53], C. Pittori [52,53], F. Lucarelli [52,53], A. Bulgarelli [54], N. Parmiggiani [54],

and

G. E. Anderson[64], J. P. Anderson[57], G. Bernardi[73,74,75], J. Bolmer[42], M. D. Caballero-García[80], I. M. Carrasco[81], A. Castellón[82], N. Castro Segura[111], A. J. Castro-Tirado[55,77], S. V. Cherukuri[69], A. M. Cockeram[61], P. D'Avanzo[43], A. Di Dato[94,95], R. Diretse[89], R.P. Fender[86], E. Fernández-García[55], J. P. U. Fynbo[108], A.S. Fruchter[107] J. Greiner[42], M. Gromadzki[112], K.E. Heintz[109] I. Heywood[86,74], A.J. van der Horst[87,88], Y.-D. Hu[55,79], C. Inserra[99], L. Izzo[55], V. Jaiswal[69], P. Jakobsson[109], J. Japelj[118], E. Kankare[98], D. A. Kann[55], C. Kouveliotou[87,88], S. Klose[68], A. J. Levan[106], X. Y. Li[83,84], S. Lotti[49], K. Maguire[100], D. B. Malesani[117], I. Manulis[97], M. Marongiu[72,22], S. Martin[57,58], A. Melandri[43], M. Michałowski[59], J.C.A. Miller-Jones[64], K. Misra[70], A. Moin[65], K.P. Mooley[92,93], S. Nasri[65], M. Nicholl[113,114], A. Noschese[94], G. Novara[103,104], S. B. Pandey[70], C. J. Pérez del Pulgar[77], M.A. Pérez-Torres[55,91], D. A. Perley[61], L. Piro[49], F. Ragosta[115,116,95], L. Resmi[69], R. Ricci[73] A. Rossi[101], R. Sánchez-Ramírez[49], J. Selsing[108] S. Schulze[63], S. J. Smartt[96], I. A. Smith[60], V. V. Sokolov[78], J. Stevens[67], N. R. Tanvir[62], C. C. Thoene[55], A. Tiengo[103,104,105], E. Tremou[85], E. Troja[102,76], A. de Ugarte Postigo[55,56], A. F. Valeev[78], S. D. Vergani[90], M. Wieringa[66], P.A. Woudt[89], D. Xu[118], O. Yaron[97], D. R. Young[96],

[1]*Inst. de Astrofísica de Canarias, E-38200 La Laguna, and Universidad de La Laguna, Dpto. Astrofísica, E-38206 La Laguna, Tenerife, Spain*

[2]*Università di Udine, and INFN Trieste, I-33100 Udine, Italy*

[3]*National Institute for Astrophysics (INAF), I-00136 Rome, Italy*

[4]*ETH Zurich, CH-8093 Zurich, Switzerland*

[5]*Technische Universität Dortmund, D-44221 Dortmund, Germany*

[6]*Croatian Consortium: University of Rijeka, Department of Physics, 51000 Rijeka; University of Split - FESB, 21000 Split; University of Zagreb - FER, 10000 Zagreb; University of Osijek, 31000 Osijek; Rudjer Boskovic Institute, 10000 Zagreb, Croatia*

[7]*Saha Institute of Nuclear Physics, HBNI, 1/AF Bidhannagar, Salt Lake, Sector-1, Kolkata 700064, India*

[8]*Centro Brasileiro de Pesquisas Físicas (CBPF), 22290-180 URCA, Rio de Janeiro (RJ), Brasil*

[9]*Unidad de Partículas y Cosmología (UPARCOS), Universidad Complutense, E-28040 Madrid, Spain*

[10]*University of Łódź, Department of Astrophysics, PL-90236 Łódź, Poland*

[11]*Università di Siena and INFN Pisa, I-53100 Siena, Italy*

[12]*Deutsches Elektronen-Synchrotron (DESY), D-15738 Zeuthen, Germany*

[13]*Istituto Nazionale Fisica Nucleare (INFN), 00044 Frascati (Roma) Italy*

[14]*Max-Planck-Institut für Physik, D-80805 München, Germany*

[15]*Institut de Física d'Altes Energies (IFAE), The Barcelona Institute of Science and Technology (BIST), E-08193 Bellaterra (Barcelona), Spain*

[16] *Università di Padova and INFN, I-35131 Padova, Italy*

[17] *Università di Pisa, and INFN Pisa, I-56126 Pisa, Italy*

[18] *Universität Würzburg, D-97074 Würzburg, Germany*

[19] *Finnish MAGIC Consortium: Tuorla Observatory (Department of Physics and Astronomy) and Finnish Centre of Astronomy with ESO (FINCA), University of Turku, FI-20014 Turku, Finland; Astronomy Division, University of Oulu, FI-90014 Oulu, Finland*

[20] *Departament de Física, and CERES-IEEC, Universitat Autònoma de Barcelona, E-08193 Bellaterra, Spain*

[21] *Japanese MAGIC Consortium: ICRR, The University of Tokyo, 277-8582 Chiba, Japan; Department of Physics, Kyoto University, 606-8502 Kyoto, Japan; Tokai University, 259-1292 Kanagawa, Japan; RIKEN, 351-0198 Saitama, Japan*

[22] *ICRANet-Armenia at NAS RA, 0019 Yerevan, Armenia*

[23] *Inst. for Nucl. Research and Nucl. Energy, Bulgarian Academy of Sciences, BG-1784 Sofia, Bulgaria*

[24] *Universitat de Barcelona, ICCUB, IEEC-UB, E-08028 Barcelona, Spain*

[25] *also at Dipartimento di Fisica, Università di Trieste, I-34127 Trieste, Italy*

[26] *also at Port d'Informació Científica (PIC) E-08193 Bellaterra (Barcelona) Spain*

[27] *Centro de Investigaciones Energéticas, Medioambientales y Tecnológicas, E-28040 Madrid, Spain*

[28] *Faculty of Mathematics and Physics, Institute of Science and Engineering, Kanazawa University, Kakuma, Kanazawa, Ishikawa 920-1192*

[29]*Institute for Cosmic-Ray Research, University of Tokyo, 5-1-5 Kashiwanoha, Kashiwa, Chiba, 277-8582, Japan*

[30]*Department of Physics, Stockholm University, AlbaNova, SE-106 91 Stockholm, Sweden*

[31]*Department of Physics, KTH Royal Institute of Technology, AlbaNova, SE-106 91 Stockholm, Sweden*

[32]*Dipartimento di Fisica "M. Merlin" dell'Università e del Politecnico di Bari, I-70126 Bari, Italy*

[33]*Istituto Nazionale di Fisica Nucleare, Sezione di Bari, I-70126 Bari, Italy*

[34]*Department of Natural Sciences, Open University of Israel, 1 University Road, POB 808, Ra'anana 43537, Israel*

[35]*Astrophysics Office, ST12, NASA/Marshall Space Flight Center, Huntsville, AL 35812, USA*

[36]*W. W. Hansen Experimental Physics Laboratory, Kavli Institute for Particle Astrophysics and Cosmology, Department of Physics and SLAC National Accelerator Laboratory, Stanford University, Stanford, CA 94305, USA*

[37]*Laboratoire Univers et Particules de Montpellier, Université Montpellier, CNRS/IN2P3, F-34095 Montpellier, France*

[38]*Department of Physics, University of Johannesburg, PO Box 524, Auckland Park 2006, South Africa*

[39]*Science and Technology Institute, Universities Space Research Association, Huntsville, AL 35805, USA*

[40]*Center for Space Plasma and Aeronomic Research, University of Alabama in Huntsville, 320 Sparkman Drive, Huntsville, AL 35899, USA*

[41]*Space Science Department, University of Alabama in Huntsville, 320 Sparkman Drive, Huntsville, AL 35899, USA*

[42]*Max-Planck Institut für extraterrestrische Physik, Giessenbachstraße 1, 85748 Garching, Germany*

[43]*INAF - Astronomical Observatory of Brera, I-23807 Merate (LC), Italy*

[44]*Mullard Space Science Laboratory, University College London, Holmbury St. Mary, Dorking, RH5 6NT, United Kingdom*

[45]*Department of Astronomy and Astrophysics, Pennsylvania State University. 525 Davey Laboratory, University Park, PA 16802, USA*

[46]*Joint Space-Science Institute, University of Maryland, College Park, Maryland 20742, USA*

[47]*INAF Istituto di Astrofisica Spaziale e Fisica Cosmica di Palermo, via Ugo La Malfa 153, I-90146 Palermo, Italia*

[48]*Department of Astronomy and Space Sciences, Istanbul University, Fatih, 34119, Istanbul, Turkey*

[49]*INAF-IAPS, via del Fosso del Cavaliere 100, I-00133 Roma, Italy*

[50]*Univ. "Tor Vergata", Via della Ricerca Scientifica 1, I-00133 Roma, Italy*

[51]*Gran Sasso Science Institute, viale Francesco Crispi 7, I-67100 L'Aquila, Italy*

[52]*INAF-Osservatorio Astronomico di Roma, Via Frascati 33, I-00078 Monteporzio Catone, Italy*

[53]*Space Science Data Center (SSDC), Agenzia Spaziale Italiana (ASI), via del Politecnico s.n.c., I-00133, Roma, Italy*

[54]*INAF-OAS, Bologna, Italy*

[55]*Instituto de Astrofísica de Andalucía (IAA-CSIC), Glorieta de la Astronomía, s/n, E-18008, Granada, Spain*

[56]*DARK, Niels Bohr Institute, University of Copenhagen, Lyngbyvej 2, DK-2100 Copenhagen Ø, Denmark*

[57]*European Southern Observatory, Alonso de Còrdova, 3107, Vitacura, Santiago 763-0355, Chile*

[58]*Joint ALMA Observatory, Alonso de Còrdova, 3107, Vitacura, Santiago 763-0355, Chile*

[59]*Astronomical Observatory Institute, Faculty of Physics, Adam Mickiewicz University, ul. Słoneczna 36, 60-286 Poznań, Poland*

[60]*Department of Physics and Astronomy, Rice University, 6100 South Main, MS-108, Houston, TX 77251-1892, USA*

[61]*Astrophysics Research Institute, Liverpool John Moores University, 146 Brownlow Hill, Liverpool L3 5RF, UK*

[62]*Department of Physics and Astronomy, University of Leicester, University Road, Leicester LE1 7RH, UK*

[63]*Department of Particle Physics and Astrophysics, Weizmann Institute of Science, Rehovot 76100, Israel*

[64]*International Centre for Radio Astronomy Research, Curtin University, GPO Box U1987, Perth, WA 6845, Australia*

[65]*Physics Department, United Arab Emirates University, P.O. Box 15551, Al-Ain, United Arab Emirates*

[66]*Australia Telescope National Facility, CSIRO Astronomy and Space Science, PO Box 76, Ep-*

ping, NSW 1710, Australia

[67] *CSIRO Australia Telescope National Facility, Paul Wild Observatory, Narrabri NSW 2390, Australia*

[68] *Thüringer Landessternwarte Tautenburg, Sternwarte 5, 07778 Tautenburg, Germany*

[69] *Indian Institute of Space Science & Technology, Trivandrum 695547, India*

[70] *Aryabhatta Research Institute of Observational Sciences, Manora Peak, Nainital 263 001, India*

[71] *Department of Physics, University of California, 1 Shields Ave, Davis, CA 95616-5270, USA*

[72] *Department of Physics and Earth Science, University of Ferrara, via Saragat 1, I-44122, Ferrara, Italy*

[73] *INAF-Istituto di Radioastronomia, via Gobetti 101, I-40129, Bologna, Italy*

[74] *Department of Physics and Electronics, Rhodes University, PO Box 94, Grahamstown, 6140, South Africa*

[75] *South African Radio Astronomy Observatory, Black River Park, 2 Fir Street, Observatory, Cape Town, 7925, South Africa*

[76] *Department of Astronomy, University of Maryland, College Park, MD 20742-4111, USA*

[77] *Unidad Asociada Departamento de Ingeniería de Sistemas y Automática, E.T.S. de Ingenieros Industriales, Universidad de Málaga, Arquitecto Francisco Peñalosa 6, E-29071 Málaga, Spain*

[78] *Special Astrophysical Observatory, Nizhniy Arkhyz, Zelenchukskiy region, Karachai-Cherkessian Republic, 369167, Russia*

[79] *Universidad de Granada, Facultad de Ciencias Campus Fuentenueva S/N CP 18071 Granada, Spain*

[80]*Astronomical Institute of the Academy of Sciences, Boční II 1401, CZ-14100 Praha 4, Czech Republic*

[81]*Departamento de Física Aplicada, Facultad de Ciencias, Universidad de Málaga, Bulevar Louis Pasteur 31, E-29071 Málaga, Spain*

[82]*Departamento de Álgebra, Geometría y Topología, Facultad de Ciencias, Bulevar Louis Pasteur 31, Universidad de Málaga, E-29071 Málaga, Spain*

[83]*Instituto de Hortofruticultura Subtropical y Mediterránea La Mayora (IHSM/UMA-CSIC), Algarrobo Costa s/n, E-29750 Málaga, Spain*

[84]*Nanjing Institute for Astronomical Optics and Technology, National Observatories, Chinese Academy of Sciences, 188 Bancang St, Xuanwu Qu, Nanjing Shi, Jiangsu Sheng, China*

[85]*AIM, CEA, CNRS, Université Paris Diderot, Sorbonne Paris Cité, Université Paris-Saclay, F-91191 Gif-sur-Yvette, France*

[86]*Astrophysics, Department of Physics, University of Oxford, Keble Road, Oxford OX1 3RH, UK*

[87]*Department of Physics, The George Washington University, 725 21st Street NW, Washington, DC 20052, USA*

[88]*Astronomy, Physics, and Statistics Institute of Sciences (APSIS), The George Washington University, Washington, DC 20052, USA*

[89]*Inter-University Institute for Data-Intensive Astronomy, Department of Astronomy, University of Cape Town, Private Bag X3, Rondebosch 7701, South Africa*

[90]*GEPI, Observatoire de Paris, PSL University, CNRS, 5 Place Jules Janssen, 92190 Meudon, France*

[91]*Depto. de Física Teórica, Universidad de Zaragoza, E-50019, Zaragoza, Spain*

[92]*National Radio Astronomy Observatory, 1003 Lopezville Road, Socorro, NM 87801, USA*

[93]*Caltech, 1200 California Blvd., Pasadena, CA 91106, USA*

[94]*Osservatorio Astronomico 'S. Di Giacomo' - AstroCampania, I-80051, Agerola (NA), Italy*

[95]*INAF - Astronomical Observatory of Naples, I-23807 Naples (NA), Italy*

[96]*Astrophysics Research Centre, School of Mathematics and Physics, Queens University Belfast, Belfast BT7 1NN, UK*

[97]*Benoziyo Center for Astrophysics, Weizmann Institute of Science, 76100 Rehovot, Israel*

[98]*Tuorla Observatory, Department of Physics and Astronomy, University of Turku, 20014 Turku, Finland*

[99]*School of Physics & Astronomy, Cardiff University, Queens Buildings, The Parade, 25 Cardiff, CF24 3AA, UK*

[100]*School of Physics, Trinity College Dublin, Dublin 2, Ireland*

[101]*INAF - Osservatorio di Astrofisica e Scienza dello Spazio, via Piero Gobetti 93/3, 40129 Bologna, Italy*

[102]*Astrophysics Science Division, NASA Goddard Space Flight Center, 8800 Greenbelt Rd, Greenbelt, MD 20771, USA*

[103]*Scuola Universitaria Superiore IUSS Pavia, Piazza della Vittoria 15, 27100 Pavia, Italy*

[104]*INAF - IASF Milano, Via E. Bassini 15, 20133 Milano, Italy*

[105]*Istituto Nazionale di Fisica Nucleare, Sezione di Pavia, Via Bassi 6, 27100 Pavia, Italy*

[106]*Department of Astrophysics, Institute of Mathematics, Astrophysics and Particle Physics*

(IMAPP), Radboud University Nijmegen, Nijmegen, the Netherlands

[107] Space Telescope Science Institute, 3700 San Martin Drive, Baltimore, MD 21218, USA

[108] The Cosmic Dawn Centre, Niels Bohr Institute, Copenhagen University, Vibenshuset, Lyngbyvej 2, DK-2100, Copenhagen

[109] Centre for Astrophysics and Cosmology, Science Institute, University of Iceland, Dunhagi 5, 107 Reykjavík, Iceland

[110] Departamento de Astrofisica, Universidad de La Laguna, Tenerife, Spain

[111] Physics and Astronomy Department, University of Southampton, Southampton, UK

[112] Warsaw University Astronomical Observatory, Al. Ujazdowskie 4, PL-00- 478 Warszawa, Poland

[113] Institute for Astronomy, University of Edinburgh, Royal Observatory, Blackford Hill, EH9 3HJ, UK

[114] Birmingham Institute for Gravitational Wave Astronomy and School of Physics and Astronomy, University of Birmingham, Birmingham B15 2TT, UK

[115] Dipartimento di Scienze Fisiche, Universit degli studi di Napoli Federico II, Via Cinthia, Edificio N, 80126 Napoli, Italy

[116] INFN, Sezione di Napoli, Complesso Universitario di Monte S. Angelo, Via Cinthia, Edificio N, 80126 Napoli, Italy

[117] DTU Space, National Space Institute, Technical University of Denmark, Elektrovej 327, 2800 Kongens Lyngby, Denmark

[118] CAS Key Laboratory of Space Astronomy and Technology, National Astronomical Observato-

ries, Chinese Academy of Sciences, Beijing 100012, China nton Pannekoek Institute for Astron-

omy, University of Amsterdam, Science Park 904, NL-1098 XH Amsterdam, the Netherlands

Long-duration gamma-ray bursts (GRBs) originate from ultra-relativistic jets launched from the collapsing cores of dying massive stars. Radiation produced through energy dissipation within the jet (prompt emission) is detected primarily at keV-MeV energies, while that arising from subsequent generation of shock waves in the external medium (afterglow emission) is detected from radio to GeV gamma-rays, mainly comprising synchrotron radiation from high-energy electrons[1–5]. Recently, the Major Atmospheric Gamma Imaging Cherenkov (MAGIC) telescopes revealed intense, long-lasting emission between 0.2 and 1 TeV from GRB 190114C[6]. Here we present the results of our multi-frequency observational campaign, and study the evolution in time of the GRB emission across 17 orders of magnitude in energy, from 5×10^{-6} up to 10^{12} eV. The broadband spectral energy distribution is found to be double-peaked, with the TeV emission constituting a distinct spectral component that has power comparable to the synchrotron component. This newly identified component is associated with the afterglow, and is satisfactorily explained by inverse Compton upscattering of synchrotron photons by high-energy electrons. The inclusion of TeV observations in GRB studies allows robust new inferences on the energy of the emitting electrons, the jet bulk Lorentz factor, and the total energetics of the GRB. The inferred values of the afterglow model parameters are similar to those found in previous studies, favouring the possibility that inverse Compton emission is commonly produced in GRBs.

GRBs are characterised by an initial phase of bright (typical observed fluxes $10^{-7}-10^{-3}$ erg cm^{-2} s^{-1}) and highly variable ($\ll$1 second) radiation in the 0.1-1 MeV band that lasts from milliseconds to minutes, known as the *prompt* emission. For many years, following the announcement in 1973 of

their discovery[7], keV-MeV radiation was the only available window to investigate these sources. In 1997 *afterglow* emission [8] was discovered, which follows the *prompt* emission but lasts much longer, from days to months, and occurs over a broader energy range, including the soft X-ray, optical and radio bands. Long lasting emission has also been detected at $\sim$ GeV energies in a fraction of GRBs, first by *CGRO*/EGRET in a handful of cases, and more recently by *AGILE*/GRID and *Fermi*/LAT (see [9] for a recent review). In the past, a hint of emission at even higher energies ($\gtrsim 650$ GeV) was found by the Milagrito experiment from observations of GRB 970417A[10].

In GRBs, the observed temporal properties (such as variability and duration) of the prompt and afterglow emissions suggest that they are produced at different locations and by different mechanisms. Prompt emission is likely produced within the jet, at distances $R \sim 10^{12} - 10^{15}$ cm from the central engine, while afterglow radiation arises from shock waves (external shocks) that occur farther out ($R > 10^{15}$ cm), caused by the interaction of the ultra-relativistic jet with the external medium [1–5]. The total amount of energy released in radiation during the prompt emission phase is typically between $\sim 10^{50}$ and $\sim 10^{51}$ erg (assuming that the radiation is beamed into a conical geometry with an opening angle of a few degrees, as commonly inferred for long-duration GRBs). The energy released during the afterglow phase is on average ten times smaller, suggesting that most of the energy is emitted during the prompt phase. The energy ratio between the prompt and afterglow phases is an important quantity, as it constrains the efficiency of the mechanism producing the prompt radiation, whose nature is still largely unknown[5].

The origin of the afterglow emission in GRBs, observed from the radio to the $\sim$ GeV band,

is in general better understood. Synchrotron radiation from electrons accelerated by collisionless processes in the external forward shock, which propagates into the ambient medium[11–14] usually provides an explanation for most of the detected radiation (a contribution from the reverse shock is sometimes evident at early times). As a consequence, the spectral and temporal characteristics of the afterglow forward shock radiation are determined by several factors, such as the properties of the jet, the properties of the external medium, and the (largely unknown) microphysics of particle acceleration and magnetic field amplification in relativistic shocks. Although afterglow radiation offers a potentially powerful probe of such aspects, most studies can rely on information on a limited range of the electromagnetic spectrum, leading to insufficient constraints on the relatively large number of free parameters in the model and the degeneracies among them. A multi-wavelength approach has proven critical to overcome these limitations [15].

On 14 January 2019, following an alert from the Neil Gehrels Swift Observatory (hereafter *Swift*) and the *Fermi* satellites, MAGIC observed and detected radiation up to at least 1 TeV from GRB 190114C. This detection opens a new window in the electromagnetic spectrum for the study of GRBs[6]. Its announcement[16] triggered an extensive campaign of follow-up observations. Owing to the relatively low redshift $z = 0.4245 \pm 0.0005$ (see Methods) of the GRB (corresponding to a luminosity distance of ~ 2.3 Gpc) a comprehensive set of multi-wavelength data could be collected. We present observations gathered from instruments onboard six satellites and 15 ground telescopes (radio, submm and NIR/optical/UV and very high energy gamma-rays; see Methods) for the first ten days after the burst. The frequency range covered by these observations spans more than 17 orders of magnitude, from 1 to $\sim 2 \times 10^{17}$ GHz, the most extensive to date for a GRB. The

light curves of GRB 190114C at different frequencies are shown in Fig. 1.

The prompt emission of GRB 190114C was simultaneously observed by several space missions (see Methods), covering the spectral range from 8 keV to ~ 100 GeV. The light curves show a complex temporal structure, with several emission peaks (Methods; Extended Data Fig. 1), with total duration ~ 25 s (see dashed line in Fig. 1) and total radiated energy $E_{\gamma,\rm iso} = (2.5 \pm 0.1) \times 10^{53}$ ergs [17] (isotropic equivalent in the energy range 1-10000 keV). During the time of inter-burst quiescence at $t \sim [5 - 15]$ seconds and after the end of the last prompt pulse at $t \gtrsim 25$ s, the flux decays smoothly, following a power law in time $F \propto t^{\alpha}$, with $\alpha_{10-1000\rm keV} = -1.10 \pm 0.01$ [17]. The temporal and spectral characteristics of this smoothly varying component support an interpretation in terms of afterglow synchrotron radiation[17,18], making this one of the few clear cases of afterglow emission detected in the band $10 - 10^4$ keV during the prompt emission phase. The onset of the afterglow synchrotron component is then estimated to occur around $t \sim 5 - 10$ s [17,18], implying an initial bulk Lorentz factor between 300 and 600 (Methods).

After about one minute from the start of the prompt emission, two additional high-energy telescopes began observations: MAGIC and the XRT, onboard *Swift*. The XRT and MAGIC light curves (1-10 keV, blue data points in Fig. 1, and 0.3-1 TeV, green data points, respectively) decay with time as a power law, and display the following decay rates: $\alpha_{\rm X} \sim -1.36 \pm 0.02$ and $\alpha_{\rm TeV} \sim -1.51 \pm 0.04$. The 0.3-1 TeV light curve shown in Fig. 1 was obtained after correcting for attenuation by the extragalactic background light (EBL)[6]. The TeV-band emission is observable until ~ 40 minutes, which is much longer than the nominal duration of the prompt emission phase.

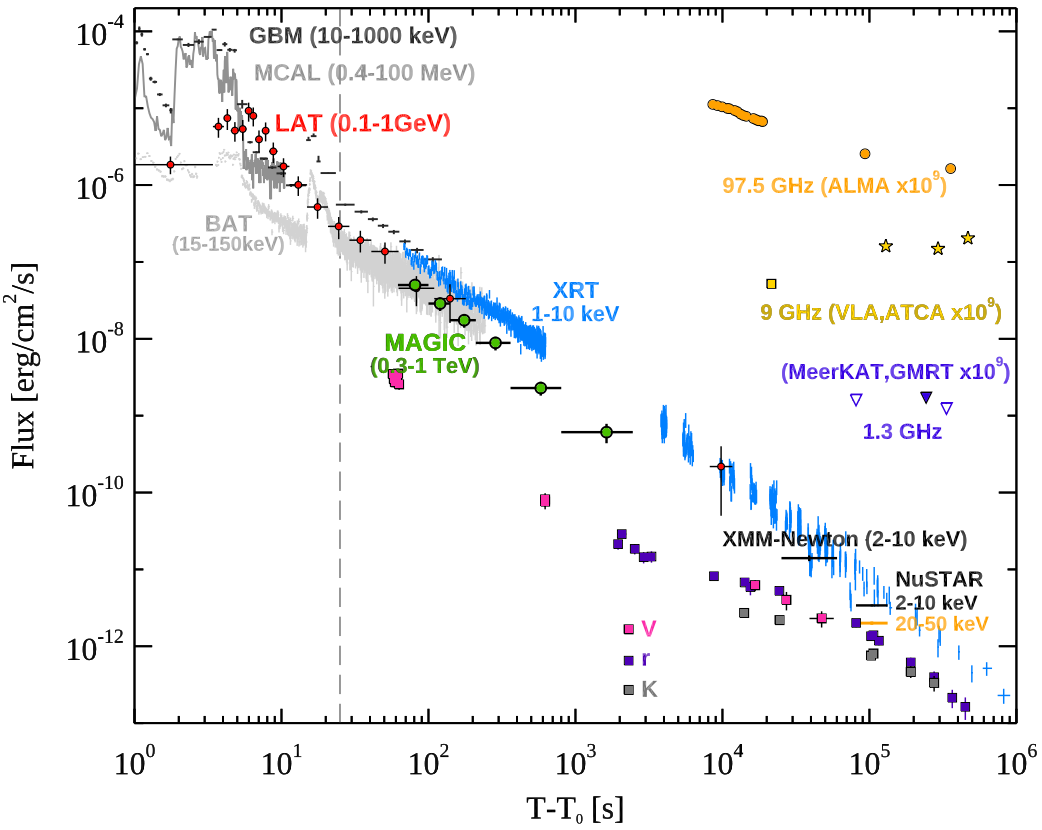

Figure 1: **Multi-wavelength light curves of GRB 190114C.** Energy flux at different wavelengths, from radio to gamma-rays, versus time since the BAT trigger time $T_0 = 20:57:03.19UT$ on 14 January 2019. The light curve for the energy range 0.3-1 TeV (green circles) is compared with light curves at lower frequencies. Those for VLA (yellow square), ATCA (yellow stars), ALMA (orange circles), GMRT (purple filled triangle), and MeerKAT (purple empty triangles) have been multiplied by 10^9 for clarity. The vertical dashed line marks approximately the end of the prompt emission phase, identified with the end of the last flaring episode. For the data points, vertical bars show the 1-σ errors on the flux, while horizontal bars represent the duration of the observation.

The NIR-optical light curves (square symbols) show a more complex behaviour. Initially, a fast decay is seen, where the emission is most likely dominated by the reverse shock component[19]. This is followed by a shallower decay, and subsequently a faster decay at $\sim 10^5$ s. The latter behaviour is not atypical, and usually indicates that the characteristic synchrotron frequency $\nu_{\rm m}$ is crossing the optical band. The millimeter light curves (orange symbols) also show an initial fast decay where the emission is dominated by the reverse shock, followed by emission at late times with nearly constant flux (Extended Data Fig. 10). All the properties of these multi-wavelength observations, from radio to GeV energies, can be explained as synchrotron afterglow emission in the context of reverse-forward shock radiation (see Methods), and provide the general framework for the investigation of the nature of the TeV emission.

The spectral energy distributions (SEDs) of the radiation detected by MAGIC are shown in Fig. 2, where the whole duration of the emission detected by MAGIC is divided into five time intervals. For the first two time intervals, observations in the GeV and X-ray bands are also available. During the first time interval (68-110 s, blue data points and blue confidence regions), *Swift*/XRT-BAT and *Fermi*/GBM data show that the afterglow synchrotron component is peaking in the X-ray band. At higher energies, up to $\lesssim$ GeV, the SED is a decreasing function of energy, as supported by the *Fermi*/LAT flux between 0.1 and 0.4 GeV (see Methods). On the other hand, at even higher energies, the MAGIC flux above 0.2 TeV implies a spectral hardening. This evidence is independent from the EBL model adopted to correct for the attenuation (Methods). This demonstrates that the newly discovered TeV radiation is not a simple extension of the known afterglow synchrotron emission, but rather a separate spectral component that has not been clearly seen before.

The extended duration and the smooth, power-law temporal decay of the radiation detected by MAGIC (see green data points in Fig. 1) suggest an intimate connection between the TeV emission and the broadband afterglow emission. The most natural candidate is synchrotron self-Compton (SSC) radiation in the external forward shock[20]: the same population of relativistic electrons responsible for the afterglow synchrotron emission Compton upscatters the synchrotron photons, leading to a second spectral component that peaks at higher energies. TeV afterglow emission can also be produced by hadronic processes such as synchrotron radiation by protons accelerated to ultra-high energies in the forward shock[21–23]. However, due to their typically low efficiency of radiation[5], reproducing the luminous TeV emission as observed here by such processes would imply unrealistically large power in accelerated protons[6]. TeV photons can also be produced via the SSC mechanism in internal shock synchrotron models of the prompt emission. However, numerical modeling (Methods) shows that prompt SSC radiation can account at most for a limited fraction ($\lesssim 20\%$) of the observed TeV flux, and only at early times ($t \lesssim 100\,\mathrm{s}$). Henceforth, we focus on the SSC process in the afterglow.

SSC components have been often observed in other types of astrophysical sources, such as blazars and pulsar wind nebulae, and had also been predicted for GRB afterglows[9,14,20,22,24–30]. However, their quantitative significance for the latter was uncertain, as their luminosity and spectral properties depend strongly on the physical conditions in the emission region that were poorly constrained. The newly detected TeV component in GRB 190114C offers the first opportunity to investigate the relevant physics at a deeper level.

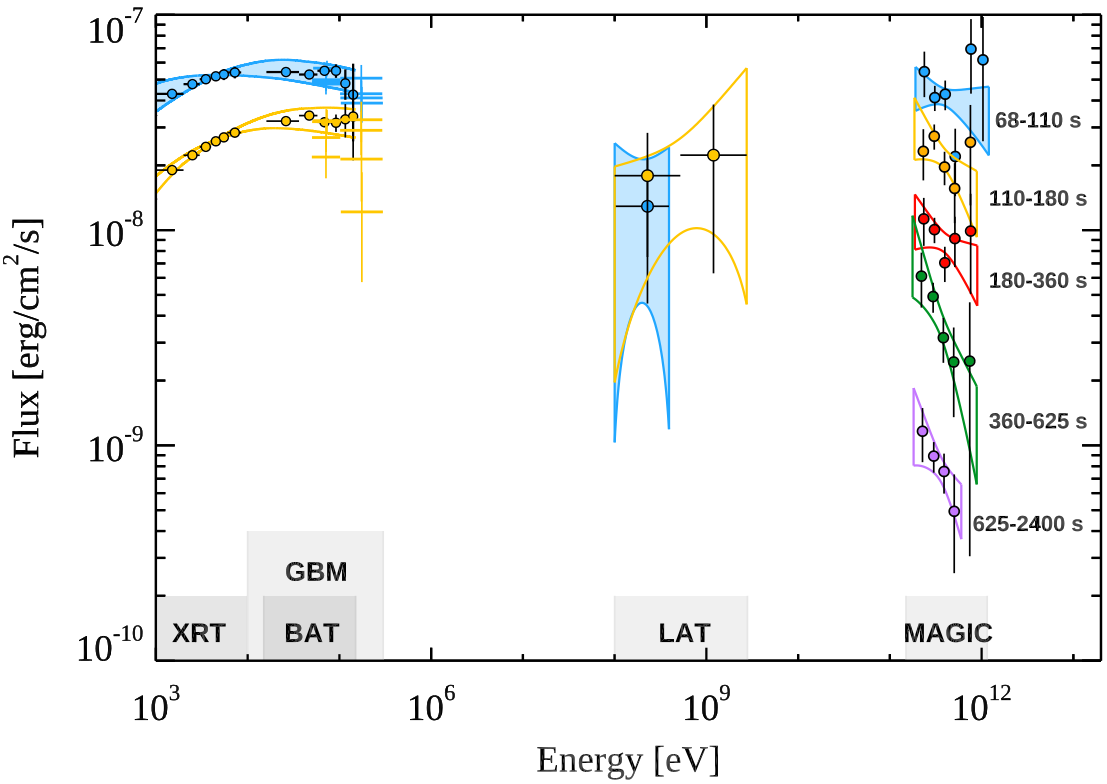

Figure 2: **Broadband spectra in the time interval 68-2400 s**. Five time intervals are considered: 68-110 s (blue), 110-180 s (yellow), 180-360 s (red), 360-625 s (green), 625-2400 s (purple). MAGIC data points have been corrected for attenuation caused by the Extragalactic Background Light. Data from other instruments are shown for the first two time-intervals: *Swift*/XRT, *Swift*/BAT, *Fermi*/GBM, and *Fermi*/LAT. For each time interval, LAT contour regions are shown limiting the energy range to the range where photons are detected. MAGIC and LAT contour regions are drawn from the 1-σ error of their best-fit power law functions. For *Swift* data, the regions show the 90% confidence contours for the joint fit XRT-BAT obtained fitting to the data a smoothly broken power law. Filled regions are used for the first time interval (68-110 s, blue color).

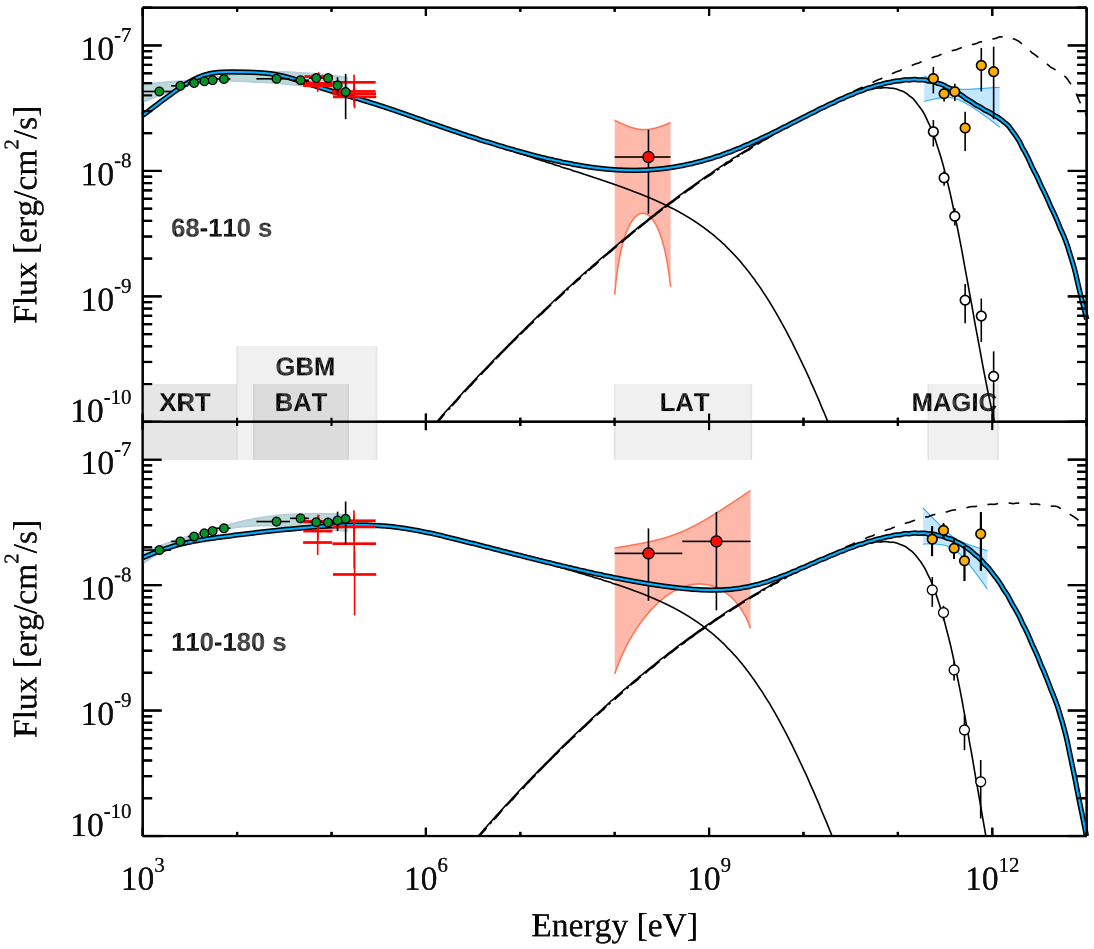

Figure 3: **Modeling of the broadband spectra in the time intervals 68-110 s (upper panel) and 110-180 s (lower panel) demonstrate that both a synchrotron and SSC component are necessary to explain the observed spectra.** Thick blue curve: modeling of the broadband data in the synchrotron and SSC afterglow scenario. Thin solid lines: synchrotron and SSC (observed spectrum) components; dashed lines: SSC if internal γ-γ opacity is neglected. For the adopted parameters, see the Text. Empty circles show the observed MAGIC spectrum, i.e. not corrected by attenuation caused by the Extragalactic Background Light. Contour regions and data points as in Fig. 2.

With this aim, we model the full data set (from radio band to TeV energies, for the first week after the explosion) as synchrotron plus SSC radiation, within the framework of the theory of afterglow emission from external reverse-forward shocks. The detailed modeling of the broadband emission and its evolution with time is presented in Section Methods. We discuss here the implications for the early time ($t < 2400\,\mathrm{s}$), high energy ($> 1\,\mathrm{keV}$) emission. Information inferred from late time optical data, allows to identify the peak of the synchrotron component visible in the X-ray band at $\sim 100\,\mathrm{s}$ as the characteristic frequency $\nu_{\rm m}$. The soft spectra (photon index $\Gamma_{\rm TeV} < -2$) in the 0.2-1 TeV energy range (see Extended Data Table 1) constrain the peak of the SSC component to be below this energy range. The relatively small ratio between the spectral peak energies of the SSC ($E_{\rm p}^{\rm SSC} \lesssim 200\,\mathrm{GeV}$) and synchrotron ($E_{\rm p}^{\rm syn} \sim 10\,\mathrm{keV}$) components implies a relatively low value for the minimum Lorentz factor of the electrons ($\gamma_{\rm m} \sim 2 \times 10^3$). This value is inconsistent with the observation of the synchrotron peak at $\gtrsim$keV energies, leading to the conclusion that Klein-Nishina (KN) scattering effects and/or internal opacity caused by γ-γ pair production have a substantial impact on the spectra. We find that in order to explain the soft spectrum detected by MAGIC, it is necessary to invoke KN-regime scattering for the electrons radiating at the spectral peak as well as internal γ-γ absorption.

While both effects tend to become less important with time, the spectral index in the 0.2-1 TeV band remains constant in time (or possibly evolves to softer values; Extended Data Table 1). This implies that the SSC peak energy is moving to lower energies and crossing the MAGIC energy band. This places robust constraints on the minimum energy of the electrons: $\gamma_{\rm m} = (1-5) \times 10^4$. The energy at which attenuation by internal pair production becomes important indicates that the

bulk Lorentz factor is $\sim$120-140 at $100\,$s.

An example of the theoretical modeling in this scenario is shown in Fig. 3 (blue solid curve, see Methods for details). The dashed line shows the SSC spectrum when internal absorption is neglected. The thin solid line shows the model spectrum including EBL attenuation, in comparison to MAGIC observations (empty circles).

We find that acceptable models of the broadband SED can be obtained if the conditions at the source are the following: the initial kinetic energy of the blastwave is $E_{\rm k} \gtrsim 2\times10^{53}$ erg (isotropic-equivalent). At least a fraction $\xi_{\rm e} \sim 0.1$ in number of the electrons swept up from the external medium are efficiently injected into the acceleration process, and carry a fraction $\epsilon_{\rm e} \sim 0.05-0.15$ of the energy dissipated at the shock. The acceleration mechanism produces an electron population characterized by a non-thermal energy distribution, described by a power law with index $p \sim 2.4-2.5$, injection Lorentz factor $\gamma_{\rm m} = 10^4 - 5\times10^4$ and maximum Lorentz factor $\gamma_{e,\rm max} \sim 10^7$ (at $\sim 100\,$s). The magnetic field behind the shock conveys a fraction $\epsilon_{\rm B} \sim (0.2-1)\times10^{-3}$ of the dissipated energy. At $t \sim 100\,$s, corresponding to $R \sim (6-8)\times10^{16}$ cm, the density of the external medium is $n > 1\,{\rm cm}^{-3}$, and the magnetic field strength is $B \sim 1-10\,$Gauss. The latter implies that the magnetic field was efficiently amplified from values of a few μGauss that are typical of the unshocked ambient medium, due to plasma instabilities or other mechanisms[5].

The blastwave energy inferred from the modeling is comparable to the amount of energy released in the form of radiation during the prompt phase. The prompt emission mechanism must then have dissipated and radiated no more than half of the initial jet energy, leaving the other half

available for the afterglow phase. The modeling of the broadband data also allows us to infer how the total energy is shared between the synchrotron and the SSC components. SSC would be 2-3 times more energetic than synchrotron if internal γ-γ absorption is neglected, but the latter substantially affects SSC such that the resultant power in the two components are comparable. We estimate that the energy in the synchrotron and SSC component are $\sim 6.5 \times 10^{51}$ erg and $\sim 1.0 \times 10^{52}$ erg respectively in the time interval 68-110 s, and $\sim 9.6 \times 10^{51}$ erg and $\sim 1.6 \times 10^{52}$ erg respectively in the time interval 110-180 s. Thus, previous studies of GRBs may have been missing a significant fraction of their released energy that is essential for their understanding.

Finally, we note that the values of the afterglow parameters inferred from the modeling fall within the range of typical values inferred from broadband (radio-to-GeV) afterglow studies. This points to the possibility that SSC emission in GRBs may be a relatively common process that does not require special conditions to be produced with power similar to synchrotron radiation. They may be detectable in other relatively energetic GRBs, as long as their redshift is low enough to avoid severe attenuation by the EBL.

Methods

GRB 190114C initial trigger and follow-up observations On 14 January 2019, the prompt emission from GRB 190114C triggered several space telescopes, including *Fermi*/GBM[31], *Fermi*/LAT[32], *Swift*/BAT[33], Super-AGILE[34], *AGILE*/MCAL[34], *KONUS*/Wind[35], *INTEGRAL*/SPI-ACS[36], and *Insight*/HXMT[37]. The first alerts (almost contemporaneous) were promptly broadcast by *Swift*/BAT[33] and the *Fermi*/GBM[31] which set the trigger time respectively at 20:57:03.19 UT (hereafter T_0) and at 20:57:02.626.Triggered by the alerts, many other instruments reported the observation and detection of GRB 190114C at different wavelengths. The multi-wavelength extensive campaign involved nearly 40 satellite and ground-based instruments covering from very high energy gamma-rays to radio. The redshift measurement was first provided by the Nordic Optical Telescope[38] and later refined by Gran Telescopio Canarias[39] to the final value $z = 0.4245 \pm 0.0005$.

Prompt emission observations A brief description of prompt observations from *AGILE*, *Fermi*, and *Swift* is reported below, and the prompt emission light curves are shown in Fig. 1 and in Extended Data Fig. 1. The emission has a complex temporal structure but three main episodes can be identified: a first episode up to 2 s, a second episode between 2 and 6 s and a third episode between 15 and 25 s. The first episode is not present in the high-energy light curves (MCAL>1.4 MeV and LAT). A delay in the onset of the high-energy component is a common feature in GRBs detected by LAT[40]. Emission is detected by BAT, GBM, and LAT also well after 25 s (see Fig. 1), however this emission is interpreted as afterglow radiation. Nominally, the T_{90}, i.e. the time interval during which a fraction between 5% and 95% of the total emission is observed, for this GRB is very long (> 100 s, depending on the energy range and instrument[17]). This quantity is generally used as

an estimate for the duration of the prompt emission. For this particular GRB, the estimate of T_{90} is contaminated by the afterglow component and does not provide a good measure of the actual duration of the prompt emission. The prompt emission lasts approximately for 25 s, where the last flaring emission episode ends. A more detailed study of the prompt emission phase is reported in [17].

AGILE The Astrorivelatore Gamma ad Immagini LEggero (AGILE) [41] is an Italian satellite devoted to high-energy astrophysics, housing a Gamma Ray Imaging Detector (GRID, 30 MeV – 30 GeV), a non-imaging Mini-CALorimeter (MCAL, 400 keV – 100 MeV), a hard X-ray coded mask detector (Super-AGILE, 20–60 keV), and an Anti-Coincidence system used for charged particle background rejection (50–200 keV). *AGILE* currently spins around its satellite-Sun axis, allowing the on-board imaging detectors to observe about 80% of the accessible sky every 7 minutes.

The localization region of GRB 190114C was accessible to *AGILE* until T_0+330 s, before becoming occulted by the Earth for the successive $\sim$45 min. GRB 190114C triggered the MCAL 16 ms and 64 ms logic timescales at $T_0-0.52$ s, issuing a data acquisition from T0-0.95 s to T0$+10.95$ s. The reconstructed light curve shows a multi-peaked burst profile lasting $T_{90} \sim 4.5$ s. No other successive on-board triggers were issued. The Super-AGILE detector also detected the burst, but the very large off-axis angle prevented any X-ray imaging of the burst, as well as spectral analysis.

Panels **a**, **d**, and **f** in Extended Data Fig. 1 show the GRB 190114C light curves acquired by the Super-AGILE detector ($20 - 60$ keV) and by the MCAL detector in the low- ($0.4 - 1.4$ MeV)

and high-energy ($1.4 - 100$ MeV) bands.

The MCAL light curve exhibits an excess of high-energy ($E > 1.4$ MeV) counts for $t > T_0 + 1.8$ s: as a consequence, the MCAL light curve in flux units is produced by using two different spectral models, fitted by using the XSPEC CSTAT statistic, a modified version of the Cash statistic used for poisson-like data on a poisson-like background. The first spectral fit was performed from $T_0-0.95$ s to $T_0+1.8$ s, adopting a power law with photon index $\Gamma_{\rm ph}$ = -1.97$^{+0.47}_{-0.70}$ (reduced χ^2 = 1.08 for 86 d.o.f.), retrieving a flux of 1.1×10^{-5} erg cm^{-2} s^{-1}, whereas the second spectral fit was performed from $T_0+1.8$ s to $T_0 + 5.5$ s with a broken power law with photon indices $\Gamma_{\rm ph,1} = -1.87^{+0.54}_{-0.19}$ and $\Gamma_{\rm ph,2} = -2.63^{+0.07}_{-0.07}$, and break energy $E_{\rm b}$ =756$^{+137}_{-159}$ keV (reduced χ^2 = 1.25 for 86 d.o.f.), retrieving a flux of 3.9×10^{-5} erg cm^{-2} s^{-1}. The total burst fluence, integrated on 6.45 s in the 0.4$-$100 MeV energy range, is equal to $F = 1.75\times10^{-4}$ erg cm^{-2}.

At T_0, GRB 190114C was about 73° off-axis, outside the GRID FoV. However, the source region was exposed before (~ 155 s, from $T_0 - 170$ s to $T_0 - 15$ s) and after the T_0 ($\sim$40 s, from $T_0 + 290$ s to $T_0 + 330$ s). In a region of $\sim 15°$ around the GRB source region, no significant signal was detected for both time intervals. A 2σ upper limit flux of 1.7×10^{-8} ph cm^{-2} s^{-1} is obtained for a time interval of $\sim$220 s (from $T_0 - 220$ s to T_0).

***Fermi*/GBM** The *Fermi*-Gamma-ray Burst Monitor (GBM) is one of the most prolific detectors for GRBs. It is composed of 12 sodium iodide (NaI, energy range: 8 keV to 1 MeV) and two bismuth germanate (BGO, 150 keV to 40 MeV) detectors [42]. GRB 190114C is among the 5 brightest GRBs observed by GBM both considering the time integrated energy and the peak photon flux [43]. The

GBM detectors pointing closest to the GRB location and thus with the brightest signal are NaI detectors number 3, 4, 7, 8, and both BGO detectors. We construct the light curve (Extended Data Fig. 1, panel **c**) by summing photon counts for the bright NaI detectors with energies between 10 and 1000 keV. The light curve consists of multiple overlapping pulses, with the bulk of the energy emitted in the first 6 seconds [17]. From T_0+25 s until about T_0+200 s, thus during the early MAGIC observations, the GBM light curve is characterised by a smooth decay of photon number as a function of time.

Spectral analysis is performed using the official GBM spectral analysis software RMFIT v4.4.2BA. At the time of the MAGIC observations there are indications that some of the detectors are partially blocked by structure on the *Fermi* Spacecraft that is not modeled in the GBM detectors' response. This affects the low-energy part of the spectrum [44]. For this reason, out of caution we elected to exclude the energy channels below 50 keV. We find that the spectra during the T_0+68 s to T_0+110 s and T_0+110 s to T_0+180 s intervals are best described by a power law model (differential photon number spectrum, $dN/dE \propto E^{\Gamma_{\rm ph}}$) with photon index $\Gamma_{\rm ph} = -2.10 \pm 0.08$ and $\Gamma_{\rm ph} = -2.05 \pm 0.10$ respectively (Figs. 2 and Extended Data Fig. 11). The photon fluxes in the canonical 10-1000 keV range for the two intervals are 3.32$\pm$0.36 photons cm^{-2} s^{-1} and 1.73$\pm$0.24 photons cm^{-2} s^{-1} respectively. We construct the flux light curve (Fig. 1) by binning the photons with signal-to-noise ratio of 70 during the bright phase (before 6 s) and 35 at later times. The fluxes are determined by integrating the best fitting spectral shape between 10 and 1000 keV.

***Swift*/BAT** The *Swift* Burst Alert Telescope (BAT [45]) is a highly sensitive, large field-of-view instrument designed to provide critical GRB triggers and 4-arcmin positions. It is a coded aperture imaging instrument with a 1.4 steradian field-of-view (half coded). The $15-350\,\mathrm{keV}$ mask-weighted light curve of GRB 190114C shows a multi-peaked structure that starts at $T_0 \sim -7\,\mathrm{s}$ (Extended Data Fig. 1, panel **b**). The brightest emission contains two complex pulses and ends at $T_0 \sim 50\,\mathrm{s}$. Afterwards, the emission appeared to decay exponentially out to beyond $T_0 \sim 720\,\mathrm{s}$, when the burst went out of the BAT field of view [46]. The burst did not come back into the BAT field of view until $T_0 \sim 3800\,\mathrm{s}$, and nothing significant was detected at that time [46]. We analysed *Swift*/BAT data and processed them with the standard *Swift* analysis software included in the NASA's HEASARC software (HEASOFT, ver.6.25) and the relevant calibration files. The 15-150 keV lightcuve is shown in Extended Data Fig. 1 (panel **b**). We extracted $15-150\,\mathrm{keV}$ BAT spectra and response matrices with the `batbinevt` tasks in FTOOLS in three time intervals (with respect to T_0): $68-180\,\mathrm{s}$, $68-110\,\mathrm{s}$ and $110-180\,\mathrm{s}$. In these time intervals we carried out a broadband joint spectral analysis of *Swift*/BAT and XRT data ($1-150\,\mathrm{keV}$) using Xspec (v.12.10). The three broadband spectra can be well described by an absorbed smoothly broken power law. For all the three intervals, the smoothness parameter has been kept fixed to 1. The best-fitting parameters for the whole interval ($68-180\,\mathrm{s}$) are: column density $N_{\rm H} = (7.53^{+0.74}_{-1.74}) \times 10^{22}\,\mathrm{cm}^{-2}$ at $z = 0.42$, in addition to the galactic value of $7.5 \times 10^{19}\,\mathrm{cm}^{-2}$, low-energy spectral index $\alpha_1 = 1.21^{+0.40}_{-1.26}$, high-energy spectral index $\alpha_2 = 2.19^{+0.39}_{-0.19}$, peak energy $E_{\rm pk} > 14.5\,\mathrm{keV}$. All errors are given at 90% confidence level.

***Fermi*/LAT** The *Fermi* Large Area Telescope (LAT) is a pair-conversion telescope consisting of a 4×4 array of silicon strip trackers and cesium iodide (CsI) calorimeters covered by a segmented anti-coincidence detector to reject charged-particle background events. The LAT detects gamma rays in the energy range from 20 MeV to more than 300 GeV with a field of view (FOV) of ~ 2.4 steradians and observes the entire sky every two orbits ($\sim$3 hours) while in normal survey mode. The LAT observes many more background events than celestial gamma-rays; therefore onboard background rejection is supplemented on the ground using event class selections that are designed to facilitate study of the broad range of sources of interest [47].

The LAT detected a gamma-ray counterpart located at R.A. (J2000), Dec. (J2000) = $03^h38^m17^s$, -26°59′24″ with an error radius of 3 arcmin [48]. The burst left the LAT FoV at T_0+150 s and remained outside the LAT field of view until T_0+8600 s.

We use `gtbin` in the standard analysis tools (ScienceTools version v11r5p3)[1] to generate the count spectrum of the observed LAT signal and `gtbkg` to extract the associated background by computing the predicted counts from cataloged point sources and diffuse emission components in the region of interest. The cataloged point sources are drawn from the 3FGL catalogue and we use the publicly available[2] isotropic (iso_P8R2_TRANSIENT020_V6_v06.txt) and galactic diffuse (gll_iem_v06.fit) templates to model the diffuse emission components. The LAT instrument response was computed using `gtrspgen`. The *Fermi*-LAT data were fitted by the mean of an unbinned likelihood taking into account at the same time the signal and the background contributions.

[1] `http://fermi.gsfc.nasa.gov/ssc/`

[2] `http://fermi.gsfc.nasa.gov/ssc/data/access/lat/BackgroundModels.html`

A power law was used to describe the LAT spectra in the time bins (with respect to T_0) 68–110 s and 110–180 s, with pivot energies of, respectively, 200 MeV and 500 MeV. In each time-interval, the analysis has been performed limited to the energy range where photons have been detected. The performed fits resulted in spectral indices $\alpha_{68-110} = -2.02 \pm 0.95$ and $\alpha_{110-180} = -1.69 \pm 0.42$, and corresponding normalisations of $N_{0,68-110} = (2.02 \pm 1.31) \times 10^{-7}$ ph MeV^{-1}cm^{-2} s and $N_{0,110-180} = (4.48 \pm 2.10) \times 10^{-8}$ ph MeV^{-1}cm^{-2} s. The LAT light curve is shown in Fig. 1 (integrated in the energy range 0.1-1 GeV) and in Extended Data Fig. 1 (panel **f**, 0.1-10 GeV).

MAGIC The Major Atmospheric Gamma Imaging Cherenkov (MAGIC) is a stereo imaging instrument composed of two 17-meter diameter Cherenkov telescopes[49,50]. It is located at about 2200 meter above sea level on the island of La Palma in the Canary Islands, Spain. On 14th January 2019 at 20:57:25 UT ($T_0 + 22$ s) a transient alert report from *Swift*/BAT triggered a prompt follow up by MAGIC. The observation started from zenith angle 55.8° and azimuth angle 175.1° and stopped on 15 January 2019 at 01:22:15 UT, for a total time of 4.12 h.

We used the standard MAGIC software [50] and followed the steps optimised for the data taking under moderate moon illumination[51]. The gamma-ray Monte Carlo (MC) used in the analysis was especially generated for this observation, reproducing its trigger discriminator threshold settings, the distributions of Azimuth and Zenith of the telescope pointing and the Night Sky Background level. As normal practice in MAGIC, the analysis has been independently performed by several analysers to evaluate the consistency and the robustness of the results.

The MAGIC spectral energy distributions (SED) shown in Fig. 3 are calculated starting from

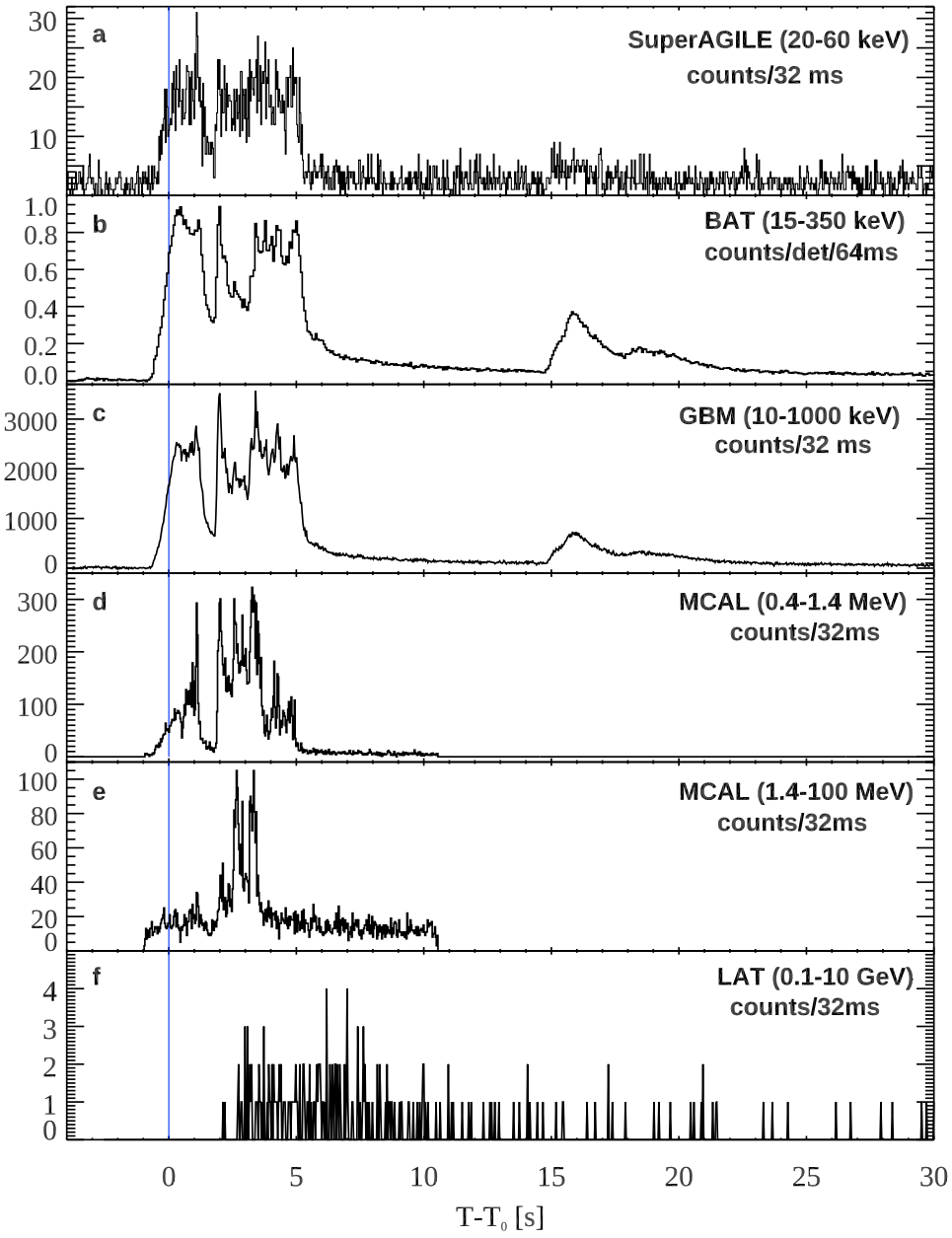

Extended Data Figure 1: **Prompt emission light curves for different detectors.** The different panels show light curves for: **a**, SuperAGILE (20-60 keV); **b**, *Swift*/BAT (15-150 keV); **c**, *Fermi*/GBM (10-1000 keV); **d**, *AGILE*/MCAL (0.4-1.4 MeV); **e**, *AGILE*/MCAL (1.4-100 MeV); **f**, *Fermi*/LAT (0.1-10 GeV). The light curve of *AGILE*/MCAL is split into two bands to show the energy dependence of the first peak. Error bars show the 1-σ statistical errors.

the differential flux distributions in reconstructed energy. The latter are obtained from the rate of the excess events divided by the effective area corrected for the spill-over effect. The differential flux points are then projected in true energy space by the use of MC and corrected for the Extra-galactic Background Light (EBL) effect[6] using the model of [52]. A fit is performed at this stage to determine the spectral shape using a user-input model. Finally the spectral points are convoluted with the best fit function to build the EBL-corrected SED in true energy.

In Extended Data Table 1 the results from the MAGIC-only time resolved spectral fitting are shown. The spectral model used to fit the MAGIC data is a power law where the normalisation and the photon index are the free parameters. The pivot energy is chosen to be close to the centre of the spectral energy range to minimise the correlation between the fitting-power-law parameters. The choice of the pivot energy is done by averaging the energies of the points weighting them with the inverse square of their relative errors. Together with the best-fit-parameter values also their statistical errors are reported. The best fit photon index values obtained in the time resolved analysis hint to a possible spectral evolution from hard to soft values. On the other hand we can not exclude that they are compatible with a constant index value of ~ -2.5 up to 2400 s. The signal and background in the considered time bins are both in the low-count Poisson regime. Therefore, the spectral fitting was treated accordingly with the proper statistics. The correct treatment of the MAGIC data provided here includes along with the Poisson statistic also the systematic errors. The main systematic error is caused by our imperfect knowledge of, among others, the absolute instrument calibration and the total atmospheric transmission resulting in a mis-match of the absolute energy scale between real and Monte Carlo data. According to dedicated studies[50] the

largest source of discrepancy is the light-scale calibration of the telescopes, which could vary, in a conservative case, by a maximum $\pm 15\%$ of the nominal value.

A time integrated SED computed for the $\pm 15\%$ light-scaled MCs and the nominal MC can be seen in Extended Data Fig. 2 that refers to the time period 62-2400 s after T_0. The statistical only error region (bow-tie) for each of the three curves is derived from the fits to the corresponding data distributions in the three light scale cases. The results of the spectral fits, including statistical errors on the parameters, are reported in Extended Data Table 1. The curves shown in Extended Data Fig. 2 for the case $\pm 15\%$ mark the extreme values of a family of equally probable curves. It is important to notice that in this family of curves the normalisation and the photon index parameters are correlated in such way that higher-flux spectra will also have harder indices. The systematic effects calculated for the time integrated spectrum can be applied to all the time resolved analysis as they would not change throughout the short period of time considered. The systematic effects deriving from the choice of one particular EBL model were also studied. The analysis performed to obtain the time integrated spectrum was repeated employing other models[53–55] to deconvolve the effect of the EBL from the spectral data. The contribution to the systematic error on the photon index caused by the uncertainty on the EBL model is $\sigma_\alpha = ^{+0.10}_{-0.13}$ which is smaller than the statistical error only (1 standard deviation) as already seen in a previous work[6]. On the other hand the contribution to the systematic error on the normalisation, due to choice of the EBL model, is only partially at the same level of the statistical error (1 standard deviation) $\sigma_N = ^{+0.30}_{-0.08} \times 10^{-8}$. The chosen EBL model returns a lower normalisation with respect to two of the other models and very close to the forth.

Time bin [seconds after T_0]	Normalisation [$\mathrm{TeV}^{-1}\,\mathrm{cm}^{-2}\,\mathrm{s}^{-1}$]	Photon index	Pivot energy [GeV]
62 - 90	$1.95^{+0.21}_{-0.20} \cdot 10^{-7}$	$-2.17^{+0.34}_{-0.36}$	395.5
68 - 180	$1.10^{+0.09}_{-0.08} \cdot 10^{-7}$	$-2.27^{+0.24}_{-0.25}$	404.7
180 - 625	$2.26^{+0.21}_{-0.20} \cdot 10^{-8}$	$-2.56^{+0.27}_{-0.29}$	395.5
68 - 110	$1.74^{+0.16}_{-0.15} \cdot 10^{-7}$	$-2.16^{+0.29}_{-0.31}$	386.5
110 - 180	$8.59^{+0.95}_{-0.91} \cdot 10^{-8}$	$-2.51^{+0.37}_{-0.41}$	395.5
180 - 360	$3.50^{+0.38}_{-0.36} \cdot 10^{-8}$	$-2.36^{+0.34}_{-0.37}$	395.5
360 - 625	$1.65^{+0.23}_{-0.23} \cdot 10^{-8}$	$-3.16^{+0.48}_{-0.54}$	369.1
625 - 2400	$3.52^{+0.47}_{-0.47} \cdot 10^{-9}$	$-2.80^{+0.48}_{-0.54}$	369.1
62 - 2400 (Nominal MC)	$1.07^{+0.08}_{-0.07} \cdot 10^{-8}$	$-2.51^{+0.20}_{-0.21}$	423.8
62 - 2400 (Light scale +15% MC)	$7.95^{+0.58}_{-0.56} \cdot 10^{-9}$	$-2.91^{+0.23}_{-0.25}$	369.1
62 - 2400 (Light scale -15% MC)	$1.34^{+0.09}_{-0.09} \cdot 10^{-8}$	$-2.07^{+0.18}_{-0.19}$	509.5

Extended Data Table 1: **MAGIC spectral fit parameters for GRB 190114C.** For each time bin, columns represent a) start time and end time of the bin; b) normalisation of the EBL-corrected differential flux at the pivot energy with statistical errors; c) photon indices with statistical errors; d) pivot energy of the fit (fixed).

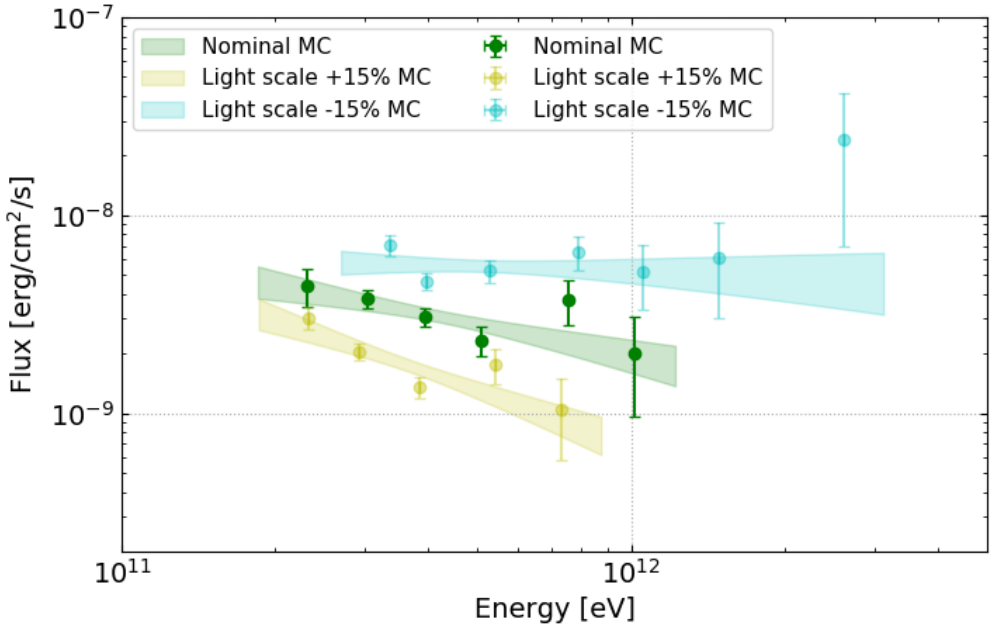

Extended Data Figure 2: **MAGIC time integrated spectral energy distributions in the time interval 62-2400 s after T_0.** The green (yellow, blue) points and band show the result with the nominal (+15%, -15%) light scale MC.

The MAGIC energy flux light curve that is presented in Fig. 1 was obtained by integrating the best fit spectral model of each time bin from 0.3 to 1 TeV. The flux errors were calculated by propagating the errors on the two spectral parameters (normalisation and photon index) and by taking into account their correlation through the covariance matrix. The energy flux light curve is fitted with a power law of the type $\sim t^{\alpha}$ where the time constant is found to be -1.51 ± 0.04. The value of the time constant reported here differs less than two standard deviation from the one previously reported[6]. The difference is due to the poor constraints on the spectral fit parameters of the last time bin, which influences the light curve fit. Because of the large temporal bins and the rapid decay of the energy flux light curve, its fitting was performed using the integral of the flux in the temporal bins instead of taking the average flux values in the middle of the time bin.

X-ray afterglow observations Observations in soft X-rays are available from *Swift*/XRT, XMM-Newton and *NuSTAR*. Observations and data reduction are described in the following sections.

***Swift*/XRT** The *Swift* X-Ray Telescope (XRT) automatically repointed its narrow field instrument and started observing 68 s after the event. Observations started in Windowed Timing mode and after 5.5 ks turned into Photon Counting mode, as the source count rate decreased appreciably. The source light curve[3] was taken from the *Swift*/XRT light curve repository [56] and converted into 1-10 keV flux (Fig. 1) through dedicated spectral fits. The combined spectral fit XRT+BAT used in Figs. 2 and 3 has been described in detail in the section describing BAT observations and analysis.

[3] https://www.swift.ac.uk/xrt_curves/00883832/

XMM-Newton The *XMM-Newton* X-ray Observatory started observing the field of GRB 190114C under a DDT ToO (observation ID: 0729161101) on Jan. 15 4:45 UT, at T_0 + 7.5 hours after the burst, till Jan. 15 20:02 UT. Data were reduced using SAS version 16.1 and the most recent calibration files. All spectra and light curves were extracted from circular regions with radii of $30''$. The background contribution was subtracted using customised regions in the same chip as the GRB afterglow. Periods of high background due to particle flares were excluded from the spectral analysis, resulting in a net exposure time of of 35, 46 and 47 ksec for the PN, MOS1 and MOS2, respectively. The flux corrected for the absorption (see Fig. 1) was derived by fitting the spectrum with XSPEC adopting a power law model with absorption in our Galaxy and at the redshift of the burst.

NuSTAR The Nuclear Spectroscopic Telescope Array (*NuSTAR*) started observing the GRB 190114C field under a DDT Target of Opportunity observation on Jan.15 19:18 UT, at T_0 + 22.5 hrs, till Jan. 17 01:12 UT. The *NuSTAR* data were reduced using the *NuSTAR* data analysis software (NuSTAR-DAS) version 1.8.0, and CALDB version 20190228. We extracted cleaned event files and spectral products using the nupipeline command, using the standard point sources extraction regions for both source and background spectra and light curves. Total exposure time was 50 ksec. The flux corrected for the absorption in two energy ranges (2-10 keV and 20-50 keV, see Fig. 1) was derived by fitting the spectrum with XSPEC using the same model implemented with XMM-Newton.

NIR, Optical and UV afterglow observations

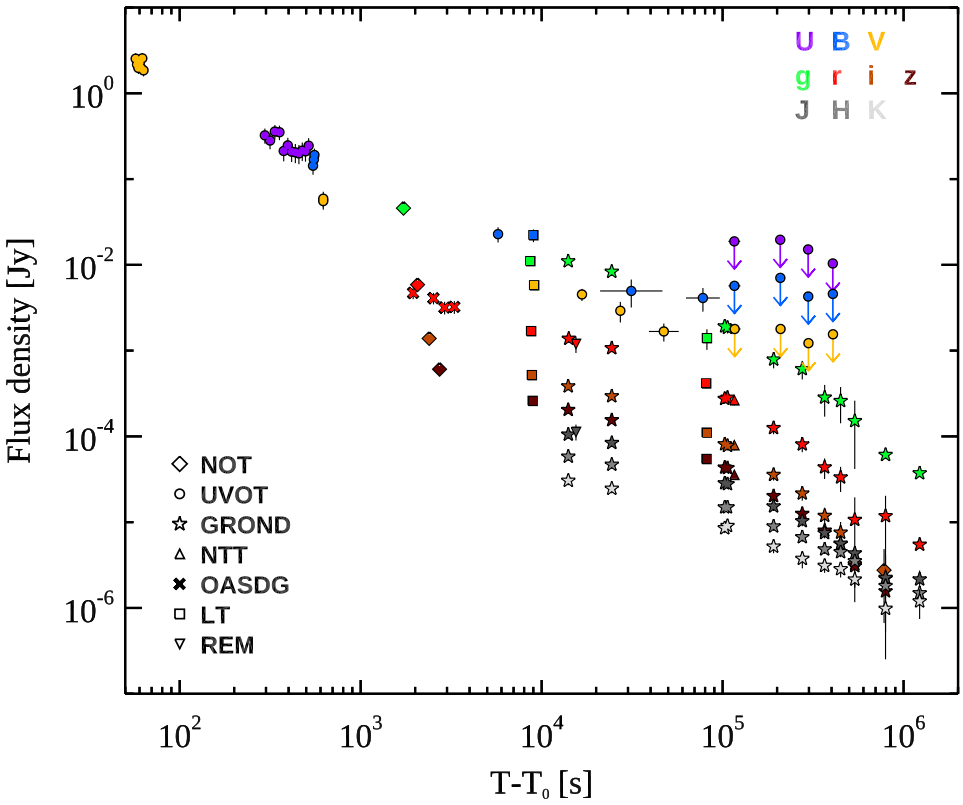

Extended Data Figure 3: **NIR/Optical/UV observations GRB 190114C.** Energy flux at different frequencies, as a function of the time since the initial burst T_0. The flux has been corrected for extinction in the host and in our Galaxy. The contribution of the host galaxy and its companion has been subtracted. Fluxes as been rescaled (except for the r filter). The change in decay rate at $\sim 3 \times 10^3$ s is caused by the transition from the fast cooling to the slow cooling regime.

GROND The Gamma-ray Burst Optical/Near-infrared Detector (GROND[57]) observations with the 7-channel NIR/Nptcal imager mounted at the 2.2 m telescope in La Silla (Chile), started around 3.8 hours after the GRB trigger, and the follow-up continued until January 29, 2019. Image reduction and photometry were carried out with standard IRAF tasks [58], as described in [59,60], and the observations were calibrated against the PanSTARRS and 2MASS stars in the field for $g'r'i'z'$and $JHK_{\rm s}$, respectively. $JHK_{\rm s}$ photometry was converted to AB magnitudes to have a common flux system. Final photometry is given in Extended Data Table 2. Flux light curves in different filters are shown in Extended Data Fig. 3 (stars).

GTC The Gran Canarias Telescope (GTC) and The all-sky cameras in Spain, the BOOTES-2 ultra-wide field camera [61], were routinely taking images of the night sky. At the GRB 190114C onset time, an image starting at3 20:57:18 UT (30 s exposure time) covered the GRB location (see Extended Data Fig. 4). Due to the proximity of the first-quarter moon, a limit of R $>$ 8 can be imposed on any prompt optical emission simultaneous to the gamma-ray prompt emission.

An optical spectrum of the GRB 190114C optical afterglow [62] was obtained with the 10.4 m GTC equipped with the OSIRIS spectrograph [63], at the Spanish island of La Palma, starting on Jan 14, 23:32 UT (2.6 hr post-burst). The grisms R1000B and R2500I were used, in order to cover the wavelength range 3,700-10,000 Å (600 s exposure times for each grism).

The GTC/OSIRIS spectrum was reduced using standard IRAF [4] routines, including debiasing and flat-fielding. The spectrum was calibrated in wavelength taking observations of arc lamps and

[4]Image Reduction Analysis Facility, distributed by the National Optical Astronomy Observatories (NOAO), which is operated by AURA Inc., under cooperative agreement with NSF

it was flux calibrated using the corresponding spectrophotometric standard star.

The calibrated spectrum from GTC/OSIRIS is shown in Extended Data Fig. 5. We detect a highly extinguished continuum, as well as CaII H and K lines in absorption, and [OII], H_β, and [OIII] in emission, all roughly at the same redshift $z = 0.4245 \pm 0.0005$ [39].

We computed the rest-frame equivalent widths (EWs) of the detected CaII absorption lines (4.2 ± 0.3 and 4.0 ± 0.2 for CaII 3934 Å and CaII 3969 Å respectively). Comparing our results with the work by [64], GRB 190114C clearly shows higher than average, but not unprecedented, values.

HST The *Hubble Space Telescope* (*HST*) imaged the afterglow and host galaxy of GRB 190114C on 11 February and 12 March 2019. At the first epoch observations in F475W, F606W, F775W and F850LP were obtained, in the second epoch usable observations were only obtained in F475W and F850LP due to a guide star acquisition failure. The *HST* observations clearly reveal that the host galaxy is a spiral (Extended Data Fig. 6), and is separated from a nearby galaxy by $\sim 1.3''$ (such that the two are blended at ground based resolution). A direct subtraction of the epochs of F850LP observations yields a faint residual close to the nucleus of the host (Extended Data Fig. 7). This is a partly unusual location to identify a long GRB since the few examples that exist within spiral galaxies are typically offset from their nuclei, although they do strongly prefer the brightest regions of their host galaxy. A precise offset is difficult to define since the apparent nucleus varies between the bands considered, likely due to differential extinction in the host galaxy. However, from the position of the residual we estimate that the burst originated within 250 pc of the host galaxy nucleus, with an uncertainty dominated by the difficulty in determining the location of the

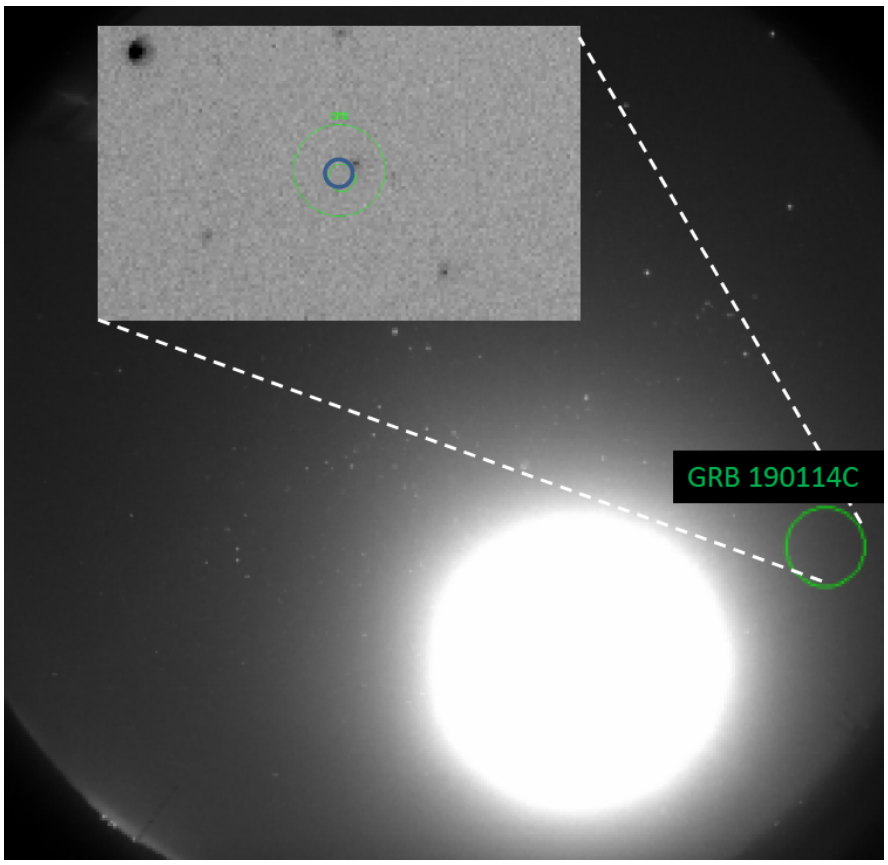

Extended Data Figure 4: **The CASANDRA-2 at the BOOTES-2 station all-sky image.** The image (30s exposure, unfiltered) was taken on Jan 14, 20:57:18 U.T. At the GRB190114C location (circle) no prompt optical emission is detected simultaneously to the gamma-ray photons (which started to arrive at 20:57:03 U.T.) See main text.

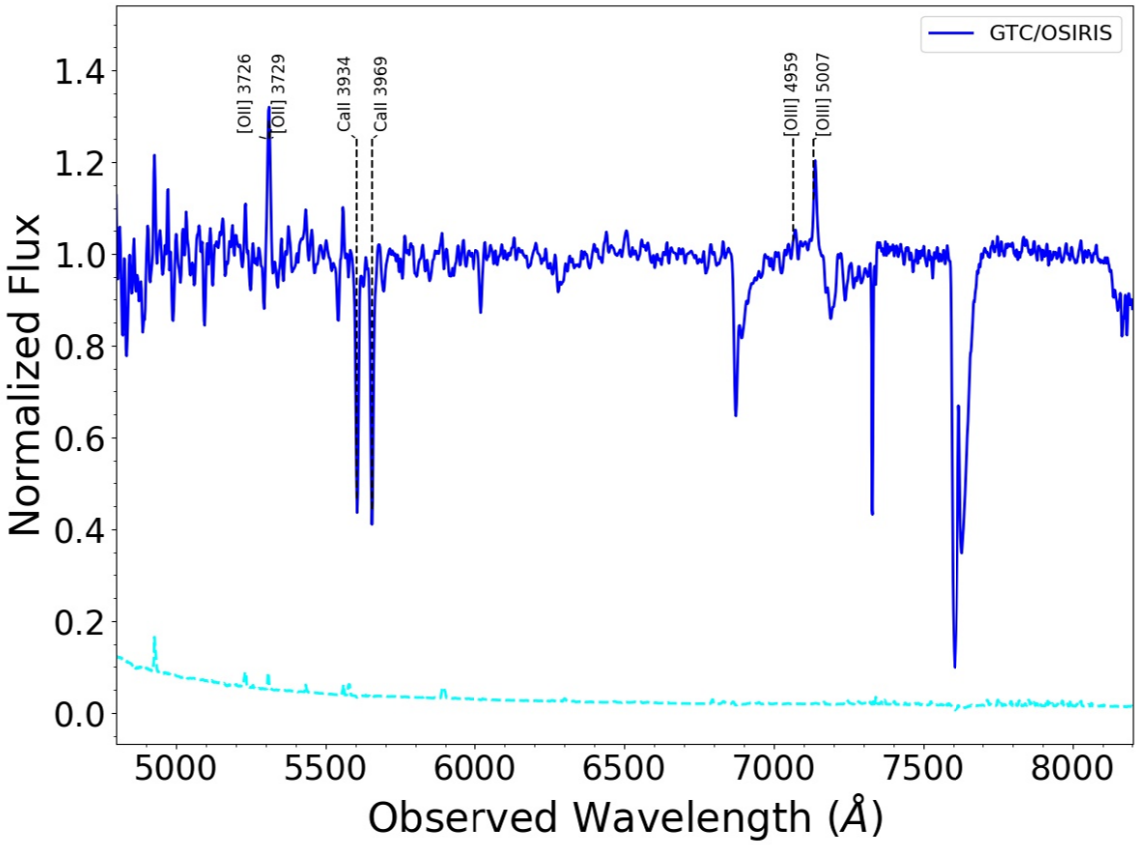

Extended Data Figure 5: **The GTC (+OSIRIS) spectrum.** The normalised spectrum of the GRB 190114C optical afterglow on Jan 14, 23:32:03 UT, taken with the R1000B and R2500I grisms. The emission lines of the underlying host galaxy are noticeable, besides the Ca II absorption lines in the afterglow spectrum (all of them are labelled). The cyan dotted line represents the noise. See main text.

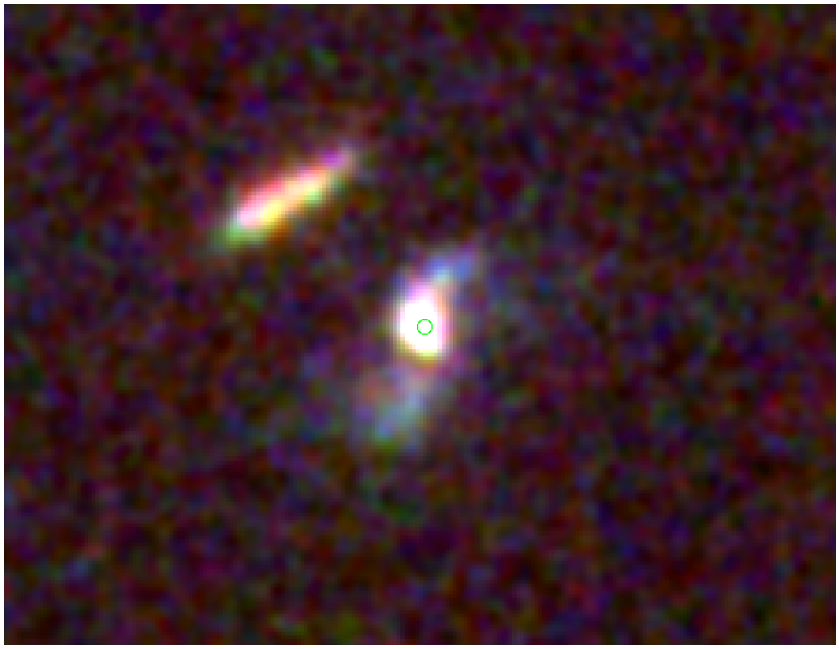

Extended Data Figure 6: **Three-colour image of the host of GRB 190114C with the HST.** The host galaxy is clearly a spiral galaxy, and the green circle indicates the location of the transient close to its host nucleus. The image is $8''$ across, north is up and east to the left.

nucleus.

LT The robotic 2-m Liverpool Telescope (LT[65]) slewed to the afterglow location at UTC 2019-01-14.974 and acquired images using the infrared-optical imager (IO:O) in B, g, V, r, i and z bands, each with 45 s exposures. On the second night, from 2019-01-15.814, three sets of 60 s exposures each were acquired in g, r, i and z bands, again with a repeated set for the r-band. All data were reduced using the standard IO:O pipeline and, where multiple exposures were performed, images were stacked using IRAF's `imcombine`. Aperture photometry of the afterglow was performed using a custom IDL script with a fixed aperture radius of $1.5''$. Photometric calibration was performed relative to stars from the Pan-STARRS1 catalogue[66]. Flux light curves in different filters

$T_{\rm GROND}$	AB magnitude						
(s)	g'	r'	i'	z'	J	H	K_s
14029.94 ± 335.28	19.21 ± 0.03	18.46 ± 0.03	17.78 ± 0.03	17.33 ± 0.03	16.78 ± 0.05	16.30 ± 0.05	16.03 ± 0.07
24402.00 ± 345.66	19.50 ± 0.04	18.72 ± 0.03	18.05 ± 0.03	17.61 ± 0.03	17.02 ± 0.05	16.53 ± 0.05	16.26 ± 0.08
102697.17 ± 524.01	20.83 ± 0.06	20.00 ± 0.04	19.30 ± 0.04	18.87 ± 0.03	18.15 ± 0.05	17.75 ± 0.06	17.40 ± 0.09
106405.63 ± 519.87	20.86 ± 0.05	19.98 ± 0.03	19.34 ± 0.03	18.88 ± 0.03	18.17 ± 0.06	17.75 ± 0.06	17.34 ± 0.09
191466.77 ± 751.37	21.43 ± 0.07	20.61 ± 0.03	19.97 ± 0.03	19.52 ± 0.03	18.77 ± 0.06	18.28 ± 0.06	17.92 ± 0.14
275594.19 ± 747.59	21.57 ± 0.07	20.88 ± 0.04	20.31 ± 0.04	19.87 ± 0.04	19.14 ± 0.07	18.57 ± 0.06	18.26 ± 0.21
366390.74 ± 1105.79	21.87 ± 0.07	21.17 ± 0.04	20.62 ± 0.03	20.15 ± 0.03	19.43 ± 0.06	18.89 ± 0.06	18.46 ± 0.15
448791.55 ± 1201.33	21.90 ± 0.08	21.27 ± 0.04	20.79 ± 0.04	20.33 ± 0.03	19.66 ± 0.07	18.97 ± 0.07	18.55 ± 0.18
537481.41 ± 1132.16	22.02 ± 0.09	21.52 ± 0.05	21.00 ± 0.04	20.55 ± 0.03	19.87 ± 0.07	19.20 ± 0.07	18.83 ± 0.17
794992.63 ± 1200.69	22.14 ± 0.04	21.51 ± 0.03	21.05 ± 0.04	20.71 ± 0.05	20.31 ± 0.13	19.79 ± 0.14	19.59 ± 0.41
1226716.84 ± 1050.15	22.17 ± 0.04	21.59 ± 0.04	21.26 ± 0.04	20.97 ± 0.04	20.34 ± 0.12	19.95 ± 0.11	19.40 ± 0.34

Extended Data Table 2: **GROND photometry.** $T_{\rm GROND}$ in seconds after the BAT trigger. The AB magnitudes are not corrected for the Galactic foreground reddening.

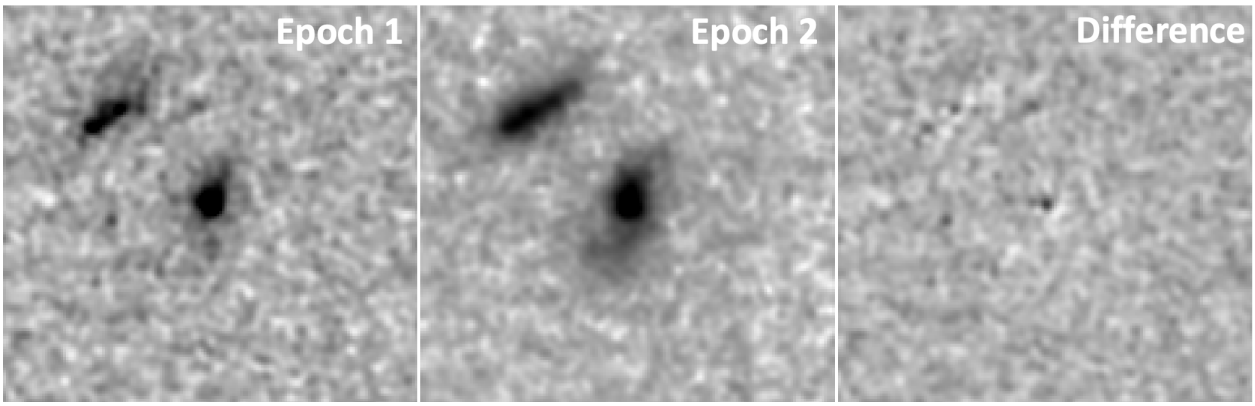

Extended Data Figure 7: **F850LP imaging of GRB 190114C taken with the HST.** Two epochs are shown (images are $4''$ across), as well as the result of the difference image. A faint transient is visible close to the nucleus of the galaxy, and we identify this as the late time afterglow of the burst.

are shown in Extended Data Fig. 3 (squares).

NTT The ESO New Technology Telescope (NTT) observed the optical counterpart of GRB 190114C under the extended Public ESO Spectroscopic Survey for Transient Objects (ePESSTO) using the NTT/EFOSC2 instrument in imaging mode [67]. Observations started at 04:36:53 UT on 2019 January 16 (i.e. about 1.32 days after the burst) and they were carried out with the g, r, i, z Gunn filters. Image reduction was carried out by following the standard procedures[68] and optical images were calibrated against the Pan-STARRS catalogue.

OASDG Optical Rc-band images of the afterglow of GRB 190114C were also obtained using the 0.5 m remote telescope of the Osservatorio Astronomico "S. Di Giacomo" (OASDG), located in Agerola (Italy). The observations started 0.54 hours after the burst, at 21:29:23 UT on 2019 January 14, and consist of a set of eight 180s multiple images. Images were corrected for the bias, the dark and the flat-field. Photometry was done against Pan-STARRS field stars catalogue and then transformed to Rc magnitudes. Although the GRB afterglow is clearly detected in all the images in the sample, the last four images were combined in order to increase the signal-to-noise of the GRB afterglow. The de-absorbed flux is shown in Extended Data Fig. 3 (crosses).

NOT The Nordic Optical Explorer (NOT) observed the optical afterglow of GRB 190114C with the 2.5 m NOT using the Alhambra Faint Object Spectrograph and Camera (AlFOSC) instrument. Imaging was obtained in the $griz$ filters with 300 s exposures, starting at Jan 14 21:20:56 UT, 24 minutes after the BAT trigger. Data were reduced using standard routines, and photometry, reported in Table 4, was calibrated to Pan-STARRS stars in the field [38].

UTC	Instrument	Filter	Exposure (s)	Magnitude
2019-01-14.975	LT/IO:O	g	45	19.08±0.06
2019-01-14.976	LT/IO:O	r	45	18.22±0.02
2019-01-14.977	LT/IO:O	i	45	17.49±0.02
2019-01-14.978	LT/IO:O	z	45	17.12±0.02
2019-01-14.979	LT/IO:O	B	45	19.55±0.15
2019-01-14.980	LT/IO:O	V	45	18.81±0.08
2019-01-15.814	LT/IO:O	r	60	19.61±0.05
2019-01-15.818	LT/IO:O	z	60	18.70±0.06
2019-01-15.820	LT/IO:O	i	60	19.04±0.04
2019-01-15.823	LT/IO:O	g	60	20.96±0.17

Extended Data Table 3: **Liverpool Telescope observations.** Magnitudes are SDSS AB-"like" for ugriz, Vega-"like" for BV and are not corrected for Galactic extinction.

UTC	t-t_0 (d)	Filter	Exposure (s)	Magnitude (AB)
2019-01-14.89127	0.0183	g	1×300	17.72±0.03
2019-01-14.89512	0.0222	r	1×300	16.93±0.02
2019-01-14.89899	0.0260	i	1×300	16.42 ±0.04
2019-01-14.90286	0.0299	z	1×300	16.17 ±0.04
2019-01-23.8896	9.0167	i	6×300	21.02±0.05

Extended Data Table 4: **Nordic Optical Explorer/AlFOSC observations.** Magnitudes are in the SDSS AB system and are not corrected for Galactic extinction.

Low-resolution spectroscopic observations with exposure time 4×300 s, also with AlFOSC, were obtained beginning Jan 14 21:47:35 UT. The normalised spectrum is shown in Fig. 8, and reveals strong host interstellar absorption lines due to Ca H & K and Na I D, which provided a redshift for the GRB of $z = 0.425$.

REM The Rapid Eye Mount telescope (REM) performed optical and NIR observations with the REM 60 cm robotic telescope equipped with the ROS2 optical imager and the REMIR NIR camera[69]. Observations were performed starting on 2019 January 15 at 00:47:35 UT (i.e. about 3.8 hours after the burst) in the r, and J bands and lasted about one hour. Image reduction, including de-biasing and flat-fielding, was carried out following standard procedures. Optical images were calibrated against the Pan-STARRS catalogue, while infrared images were calibrated using a set of 2MASS field stars. The de-absorbed flux is shown in Fig. 3 (upside down triangle).

Swift/UVOT The *Swift* UltraViolet and Optical Telescope (UVOT[70]) began at $T_0 + 54$ seconds observations) in the UVOT v band at the end of the slew, while still settling on the target. The first observation after settling started 74 s after the trigger for 150 s in the UVOT $white$ band[71]. A 50 s exposure with the UV grism was taken thereafter, followed by multiple exposures rotating through all seven broad and intermediate-band filters until switching to only UVOT's clear white filter on 2019-01-20. *Swift* observations continued until 2019-02-10. The initial exposures were in image/event mode which tags photons by position and arrival time and after 600 s in image mode only. The standard *Swift* UVOT photometric calibration and methods were used for deriving the aperture photometry[72,73]. The latest HEASARC *Swift* software "Ftools" (HEAsoft-6.25) and calibration database (*Swift* CALDB) were used for the photometry, except that for the grism zeroth

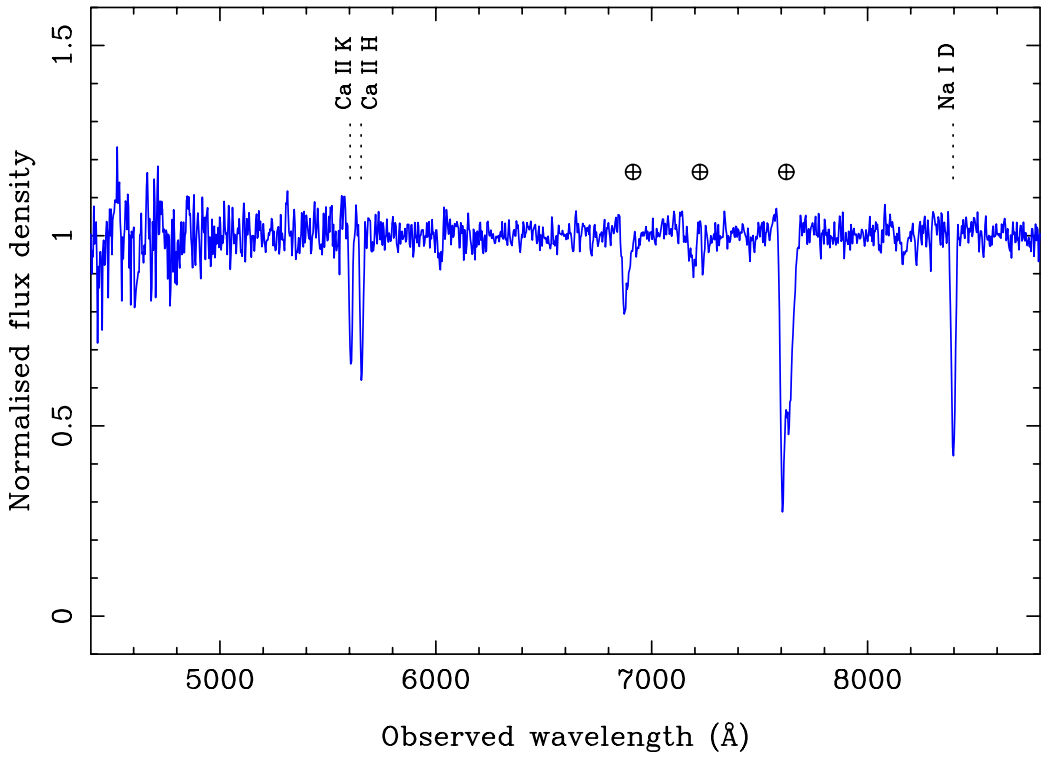

Extended Data Figure 8: **The NOT/AlFOSC spectrum.** The NOT/AlFOSC spectrum obtained at a mid-time 1 hr post-burst. The continuum is afterglow dominated at this time, and shows strong absorption features of Ca II and Na I (in addition to telluric absorption).

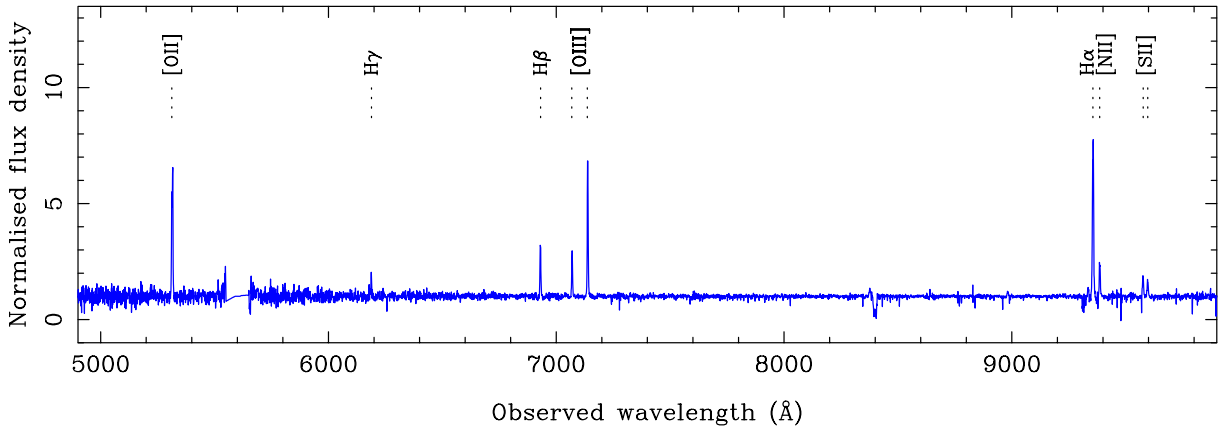

Extended Data Figure 9: **The VLT/X-shooter spectrum.** The visible light region of the VLT/X-shooter spectrum obtained approximately 3.2 d post-burst, showing strong emission lines from the star-forming host galaxy.

order the data were reduced manually[74] to derive the b-magnitude and error. Flux light curves in different filters are shown in Extended Data Fig. 3 (circles).

VLT The STARGATE collaboration used the Very Large Telescope (VLT) and observed GRB 190114C using the X-shooter spectrograph at the European Southern Observatory (ESO) at two epochs, beginning Jan 15th 01:25:16 UT and Jan 18th 00:59:32 UT. Detailed analysis of these data-sets will be presented in forthcoming papers; here we show a portion of the second spectrum (Fig. 9) illustrating the strong emission lines characteristic of a strongly star-forming galaxy, whose light is largely dominating over the afterglow at this epoch.

Magnitudes of the underlying galaxies The *HST* images show a spiral or tidally disrupted galaxy whose bulge is coincident with the coordinates of GRB 190114C. A second galaxy is detected at an angular distance of 1.3″, towards the North East. Due to the small angular separation between

these two objects, they are not properly resolved in many of the ground based images. To account for the contribution of these objects in our photometry we are using synthetic magnitudes that were derived for each of our observing filters from SED fits to the observations of both galaxies. This SED fit used photometric information in visible and near-infrared wavelengths obtained from *HST*, *HAWK-I* as well as catalogue data in the ultraviolet and mid-infrared from GALEX [75], and WISE[76], respectively. The SED analysis was performed with LePhare [77,78] using an iterative method that combined both the resolved photometry of the two objects in the *HST* and *VLT*/HAWK-I data and the blended photometry from *GALEX* and WISE, where the spatial resolution was much lower. Further details of this analysis will be given in a separate paper (de Ugate Postigo et al., in preparation). The estimated photometry for each of the objects and for the combination of them is given in Extended Data Table 5.

Optical Extinction The optical extinction toward the line of sight of a GRB can be derived assuming a synchrotron spectrum (e.g. a PL) as intrinsic spectral shape for the afterglow and one of the known recipes for the extinctions [79]. It is observed that in a large fraction of cases the extinction curve typical of the Small Magellanic Cloud works well [80], although different extinction curves are often needed particularly for the more absorbed lines of sight (e.g. $A_V \geq 2$ mag)[81]. Within the context of the broadband SED modeling of this paper, once the small Galactic extinction ($E_{\rm B-V} = 0.01$[82]) is taken into account and the fairly bright host galaxy contribution is properly subtracted, we could obtain a good fit to the data at early ($0.1-0.4$ days) and later ($1-3.5$ days) epochs both with the SMC recipe and $A_V = 1.50\pm0.11$ mag (1σ credible region), and with the LMC recipe and $A_V = 1.83 \pm 0.15$. The PL spectral index β ($F_\nu \propto \nu^{\beta_{\rm o}}$) evolves from hard to soft across the

Filter	Host	Companion	Combined
Sloan u	23.54	25.74	23.40
Sloan g	22.51	23.81	22.21
Sloan r	22.13	22.81	21.66
Sloan i	21.70	22.27	21.19
Sloan z	21.51	21.74	20.87
2MASS J	20.98	21.08	20.28
2MASS H	20.68	20.82	20.00
2MASS Ks	20.45	20.61	19.77

Extended Data Table 5: **Observations of the host galaxy.** For each filter, the estimated magnitudes are given for the host galaxy of GRB 190114C, the companion and the combination of the two objects.

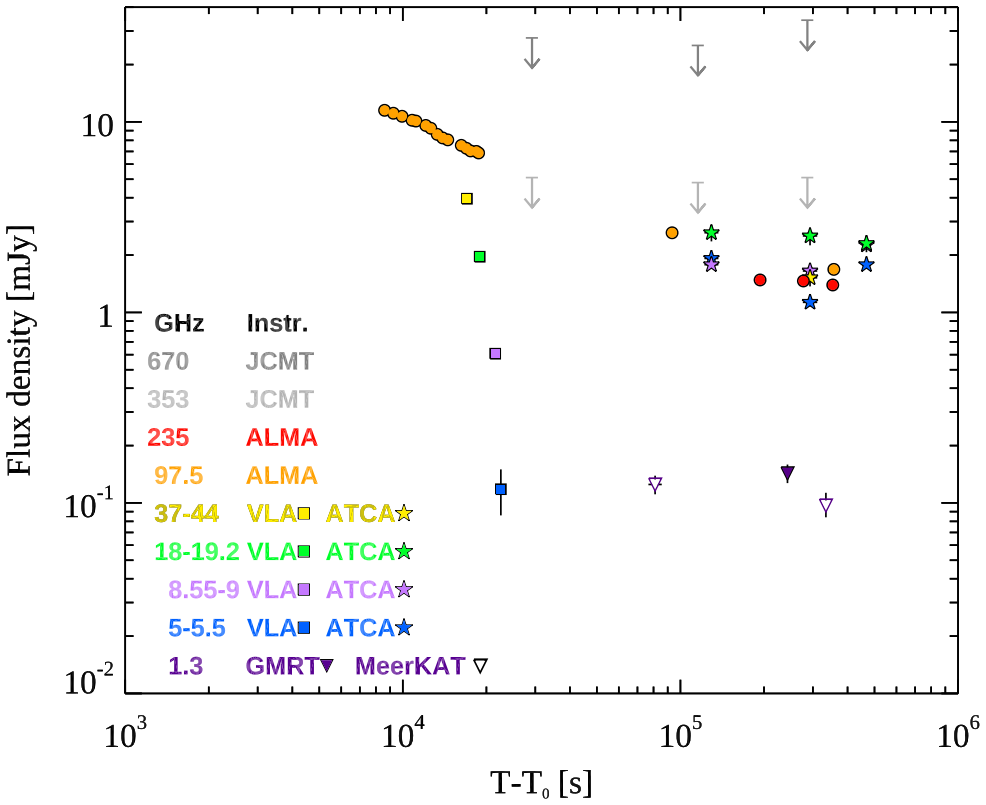

Extended Data Figure 10: **Radio and sub-mm observations GRB 190114C:** energy flux at different frequencies, from 1.3 GHz to 670 GHz, as a function of the time since the initial burst T_0.

temporal break in the optical light-curve at about 0.5 days, moving from $\beta_{o,1} = -0.48 \pm 0.10$ to $\beta_{o,2} - 0.77 \pm 0.13$ in the SMC case, and from $\beta_{o,1} - 0.10 \pm 0.12$ to $\beta_{o,2} - 0.48 \pm 0.15$ in the LMC case). Other choices for the extinction curve could also give a reasonable fit to the optical data since the extinction bump at ~ 220 nm is, at the redshift of GRB 190114C, bluer than the available photometry. Fluxes in Fig. 1, and Extended Data Figs. 3,11, 12 have been derived assuming the LMC case, since it is in better agreement with the theoretical model.

Radio and Sub-mm afterglow observations

ALMA Millimetre observations were carried out with the Atacama Large Millimetre/Submillimetre Array (ALMA) in Band 6 and Band 3 between 2019 January 15 and 2019 January 19. The configuration (C43-2) used 47-48 antennas, with baselines ranging from 15 m to 313 m ($12 - 253\ k\lambda$ in Band 7 and $5 - 105\ k\lambda$ in Band 3). Band 3 observations consisted of 8.6 minutes on source; Band 6 observations were 43 minutes on source. Weather conditions were relatively poor, with pwv $3 - 4$ mm (we also requested Band 7 observations, but these could not be executed under the available conditions). The correlator was configured for a central observed frequency of 97.500 GHz (Band 3) or 235.0487 GHz (Band 6). All data were calibrated within CASA (Common Astronomy Software Applications, version 5.4.0[83]) using the pipeline calibration. The average spatial resolution achieved was typically 2.5″ for Band 3 and 1″ for Band 6. Photometric measurements were also performed within CASA. The flux calibration was performed using J0423-0120 (for the first Band 3 epoch and the last Band 6 epoch) and J0522-3627 (for the remaining epochs). The results are shown in Extended Data Fig. 10 Red circles are used for observations at 235 GHz and orange circles for 97.5 GHz. Early time ($t < 3 \times 10^4$ s) ALMA observations at 97.5 GHz are taken from [19].

ATCA Observations with the Australia Telescope Compact Array (ATCA) were made under the project code CX424, and were run as an observatory service. Data were obtained using the CABB continuum mode [84] which provided two simultaneous bands, each with 2 GHz of bandwidth. Observations were made with the ATCA 4 cm receivers (band centres 5.5 and 9 GHz), 15 mm receivers (band centres 17 and 19 GHz), and 7 mm receivers (band centres 43 and 45 GHz). Table 6 shows

the observation epochs, and which receivers were used in each. Time-dependent gain calibration was obtained using the ATCA calibrator source 0237-233 (R.A. 02:40:08.17, Dec. -23:09:15.7), and absolute flux density calibration was made with PKS B1934-638 [85]. Data reduction was performed with the software packages MIRIAD [86] and CASA [83] using standard techniques. The final flux values were measured in both the image plane (force-fitting a Gaussian to the GRB position) and in the visibility plane to check for consistency. The quoted errors are 1σ, which include the RMS and Gaussian 1σ errors. ATCA observations at four different frequencies are shown in Extended Data Fig. 10, where they can also be compared to early time observations ($t < 3 \times 10^4$ s) performed at similar frequencies with the VLA[19].

GMRT The upgraded Giant Metre-wave Radio Telescope [87] (UGMRT) observations of GRB 190114C were carried out under the approved ToO program 35_018 on 17th January 2019 13.44 UT (2.8 days after the burst) in band 5 (1000-1450 MHz) with 2048 channels spread over 400 MHz. 3C147 was used as flux and bandpass calibrator and 0423-013 was used as phase calibrator. The data were processed and analysed using a customised pipeline (Ishwara Chandra et al., in prep.) developed under the CASA environment. Tasks *tfcrop* and *rflag* were used to flag bad data. Standard procedures were followed for calibration. The imaging was done using the task *tclean* with imsize=3400 and cellsize=0.5". The flux value was measured by fitting a Gaussian profile at the GRB position. A weak source with a flux density of 73 ± 17 μJy was detected at the GRB position [88]. We have not corrected for the flux of the host galaxy which was detected in the pre-explosion images made by MeerKAT [89]. The estimated flux should then be considered as an upper limit (upside down filled triangles in Extended Data Fig. 10).

Start Date and Time	End Date and Time	Frequency GHz	Flux mJy
1/16/2019 6:47:00	1/16/2019 10:53:00	5.5	1.92±0.06
		9	1.78±0.06
		18	2.62±0.26
1/18/2019 1:45:00	1/18/2019 11:18:00	5.5	1.13±0.04
		9	1.65±0.05
		18	2.52±0.27
		44	1.52±0.15
1/20/2019 3:38	1/20/2019 10:25:00	5.5	1.78±0.06
		9	2.26±0.07
		18	2.30±0.23

Extended Data Table 6: **Observations by ATCA**. Start and end date and times (UTC) of the observations, frequency, and flux (1σ error).

MeerKAT The long GRB 190114C was observed over two epochs with the new MeerKAT radio observatory [90,91] on 15 and 18 January 2019, with DDT requested by the ThunderKAT Large Survey Project [92]. Both epochs used 63 antennas and were done at L-band, split into 4096 frequency channels spanning 856 MHz and centered at 1284 MHz. Observations alternated between 10 minutes on source and 1-minute observations of a phase calibrator (J0240-2309), while a bandpass and flux calibrator (J0408-6545) was observed at the start and at the end of the observing blocks.

The data were flagged using AOFlagger (v2.9) [93] and calibrated following standard procedures (phase corrections, antenna delays, and bandpass corrections) with CASA (v5.1) [94]. To manage the data volume, a channel binning factor of 8 was applied, resulting in 512 channels with 1.67 MHz width each, but the 8 second time resolution remained the same. Imaging of the data was carried out with the new wide-band, wide-field imager, DDFacet [95]. DDFacet is based on a co-planar faceting scheme and it takes into account generic direction-dependent effects that dominate wide fields such as the $\sim$ 1 degree of MeerKAT. A Briggs weighting scheme (robust=-0.7) was used and the deconvolution was done over 4 frequency chunks using the SSDCLEAN deconvolution algorithm. DDFacet is accompanied by the calibration software killMS, that was used to apply self-calibration in order to correct for considerable artifacts from bright sources. The image quality was optimized by using the COHJONES (Complex Half-Jacobian Optimization for N-directional EStimation) [96] algorithm that solves for scalar Jones matrices in a user-defined number of directions and includes corrections for direction-dependent effects.

For the flux estimation, the source finding software PyBDSF v.1.8.15 [97] was used to apply source fitting. The peak flux density at the location of GRB 190114C was 125$\pm$10 μJy/beam

on 15 January and 97±12 μJy/beam on 18 January. The median synthesized beam in the L-band MeerKAT images was 5"×4". The RMS noise of the final images was 10 μJy/beam and 11 μJy/beam for January 15 and January 18, respectively. Adding the RMS noise in quadrature to the flux uncertainty leads to final flux measurements of 125±14 μJy/beam on 15 January and 97±16 μJy/beam on 18 January. Note that these flux density measurements include a contribution from the host galaxy [89]. Therefore, these measurements provide a maximum flux of the GRB (upside down empty triangles in Extended Data Fig. 10).

JCMT SCUBA-2 Sub-millimeter Sub-millimeter observations of GRB 190114C were performed simultaneously at 850 μm and 450 μm on three nights using the SCUBA-2 continuum camera[98] on the James Clerk Maxwell Telescope (JCMT) on Mauna Kea, Hawaii. The SCUBA-2 data were analysed in the standard manner using the 2018A version of Starlink[99]; this used Version 1.6.1 of SMURF[100] and Version 2.5-8 of KAPPA. Observations of the SCUBA-2 calibrator CRL 618 were performed immediately prior to observing GRB 190114C. Standard Daisy maps were made centered on the targets. Although CRL 618 was located far from GRB 190114C, its elevation was similar. The weather conditions for the calibrator and GRB 190114C observations were similar and were very good Grade 1 on all three nights. The flux conversion factors determined for the calibrator observations agreed with the standard values [101] that could then be used for the flux normalisation. In the SCUBA-2 Dynamic Interactive Map-Maker, the Blank Field map was used for the GRB 190114C observations. The maps were smoothed using a matched filter. The RMS background noise was determined in the central 2′ of the map with the source excluded. The SCUBA-2 observations of GRB 190114C are summarised in Extended Data Table 7. These ex-

pand on the preliminary results given in [102]. GRB 190114C was not detected at 850 μm or 450 μm on any of the individual nights. Combining all the SCUBA-2 observations, the RMS background noise is 0.95 mJy/beam at 850 μm and 5.4 mJy/beam at 450 μm at 1.67 days after the burst trigger (grey arrows in Extended Data Fig. 10). Despite the low elevation of the source, the limits at 450 μm are decent owing to the very good weather. Another nearby source at (03:38:03.6, –26:56:48.6) does appear to be detected by SCUBA-2, with flux densities of 6.0 mJy/beam at 850 μm and 29.7 mJy/beam at 450 μm.

Prompt emission model for the early time MAGIC emission Many observed features of GeV energy emission on the time scales shorter than the duration of the prompt MeV burst have been explained as being due to prompt radiation. In the standard picture the sub-MeV spectrum is explained as a synchrotron radiation from relativistic accelerated electrons in the energy dissipation region. Simulations have shown that magnetic fields required to produce the GeV/TeV component are rather low[103], $\epsilon_B \sim 10^{-3}$. Typically the high energy emission is sensitive also to the details of the dynamics: e.g. in the internal shock model if the peak energy is initially very high and the IC component is suppressed due to Klein-Nishina (KN) effects, the peak of the IC component may be delayed and become bright only at late times when scatterings occur in Thomson regime. Alternatively, if the prompt emission originates in reprocessed photospheric emission, the early TeV flux may arise from IC scatterings of thermal photons by freshly heated electrons below the photosphere at low optical depths. Another possibility for the generation of TeV photons might be the IC scattering of prompt MeV photons by electrons in the external forward shock region where electrons are heated to an average Lorentz factor of order 10^4 at early times. If

UT Date	Time since trigger (days)	Time on source (hours)	Typical 225 GHz CSO Opacity[a]	Typical elevation (degrees)	850 μm RMS density (mJy/beam)	450 μm RMS density (mJy/beam)
2019-01-15	0.338	1.03	0.026	39	1.7	9.2
2019-01-16	1.338	1.03	0.024	39	1.6	8.4
2019-01-18	3.318	0.95	0.031	37	1.7	11.4

Extended Data Table 7: **JCMT SCUBA-2 sub-millimeter observations of GRB 190114C.** [a]The CSO 225 GHz tau measures the zenith atmospheric attenuation.

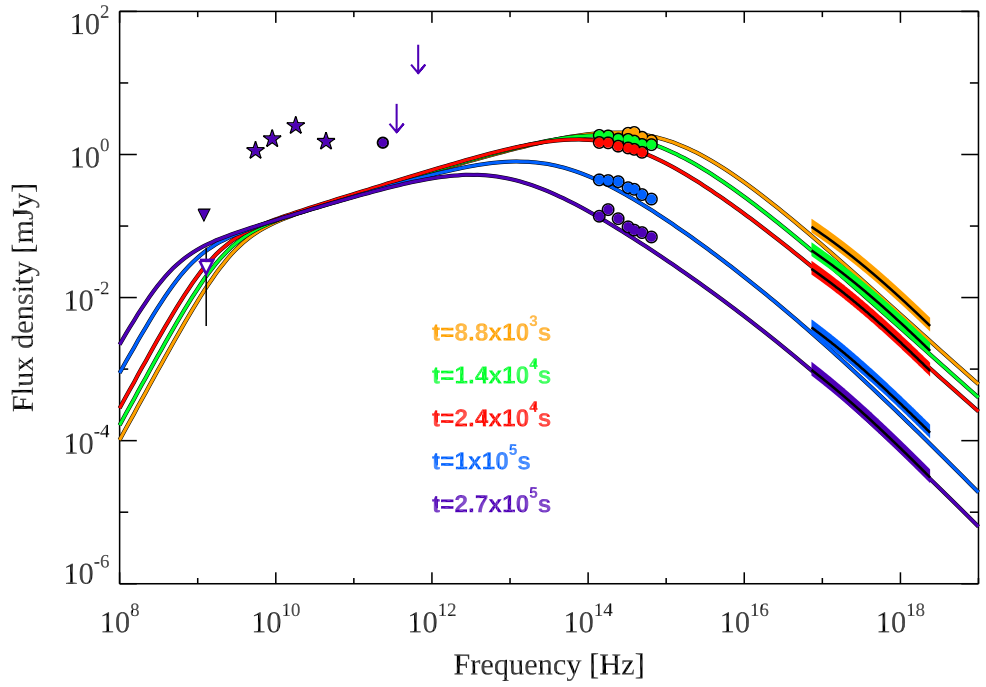

Extended Data Figure 11: **Radio to X-rays SED at different epochs**. The synchrotron frequency $\nu_{\rm m}$ crosses the optical band, moving from higher to lower frequencies. The break between 10^8 and 10^{10} Hz is caused by the self-absorption synchrotron frequency $\nu_{\rm sa}$. Optical (X-ray) data have been corrected for extinction (absorption).

the observed keV/MeV emission is interpreted as synchrotron emission in the framework of the internal shock model[103], the prompt emission simulations show that the corresponding inverse Compton component could contribute to MAGIC observations at early times ($< T_0 + 90\,\mathrm{s}$) by $\lesssim 20\%$ of the observed flux (see the 62-90 s time interval in Extended Data Table 1).

Afterglow model We discuss the broadband afterglow emission within the external shock model[12, 13, 20, 28, 104] (i.e., synchrotron and SSC radiation from electrons accelerated at the reverse/forward shock). The results of the modeling are shown in Fig. 3, Extended Data Fig. , and Extended Data Figs. 11 and 12, where we overlay the theoretical model to the data. The details on the interpretation and the information inferred from the different data sets are explained in the following subsections, divided according to the energy band.

We consider two types of radial profiles for the external environment, described by $n(R) = n_0\, R^{-s}$, with $s = 0$ describing a homogeneous medium, and $s = 2$ describing a wind-like medium (typical of an environment shaped by the stellar wind of the progenitor). In the last case, we define $n_0 = 3 \times 10^{35}\, A_\star\,\mathrm{cm}^{-1}$. We assume that a fraction ξ_e of the electrons swept up by the shock are efficiently accelerated into a PL distribution described by spectral index p: $dN/d\gamma_\mathrm{e} \propto \gamma_\mathrm{e}^{-p}$, where γ_e is the electron Lorentz factor. We call ν_m the characteristic synchrotron frequency of electrons with Lorentz factor γ_m, ν_c the cooling frequency, and ν_sa the self-absorption synchrotron frequency.

The early time optical emission (up to $\sim 1000\,\mathrm{s}$) and radio emission (up to $\sim 10^5\,\mathrm{s}$) are most likely dominated by reverse shock radiation [19]. Detailed modeling of this component is not

discussed in this work, where we focus on forward shock radiation.

X-ray emission: fitting a simple PL to the XRT light curve (Fig. 1, blue data points) we find a decay rate $F_{\rm X} \propto t^{\alpha_{\rm X}}$ with $\alpha_{\rm X} = -1.36 \pm 0.02$. A broken power law fit provides a better fit, with evidence for a break (5.3×10^{-5} probability of chance improvement) occurring around 4×10^4 s and decay indices before and after the break $\alpha_{\rm X,1} \sim -1.32 \pm 0.03$ and $\alpha_{\rm X,2} \sim -1.55 \pm 0.04$. A single PL light curve can be explained if the X-ray band lies all the time in the same part of the synchrotron spectrum. If $\nu_{\rm X} > max(\nu_{\rm X}, \nu_{\rm c})$, no matter the electron cooling regime (fast or slow cooling) and the radial profile of the external density, the X-ray light curve is predicted to decay as $t^{(2-3p)/4}$, that implies $p \sim 2.5$. Another possibility is to assume $\nu_{\rm m} < \nu_{\rm X} < \nu_{\rm c}$ for the whole observing time, which implies a slow cooling regime and $p = 2.1 - 2.2$ to explain the temporal decay. If one instead assumes that the temporal break at 4×10^4 s is significant, then the break and the temporal indices before and after can be explained only if the electrons are in a slow cooling regime at the time of the break, and assuming $p = 2.7$ (for $s = 0$) and $p = 2.4 - 2.5$ for $s = 2$. In both cases, the temporal break is caused by the cooling frequency $\nu_{\rm c}$ crossing the XRT band.

Optical emission: the contribution of the reverse shock to the optical emission lasts until $\sim 2 \times 10^3$ s [19], when the optical light curve starts displaying a shallow decay in time (with temporal index poorly constrained, between -0.5 and -0.25), followed by a steepening around 8×10^4 s, where the optical light curve displays a temporal decay similar to the decay seen in X-ray band, suggesting that the X-ray and optical band lie in the same part of the synchrotron spectrum after 8×10^4 s. A temporal break in optical is often satisfactorily explained as caused by the synchrotron characteristic frequency $\nu_{\rm m}$ crossing the optical band. After $\nu_{\rm m}$ has crossed the optical band ($t >$

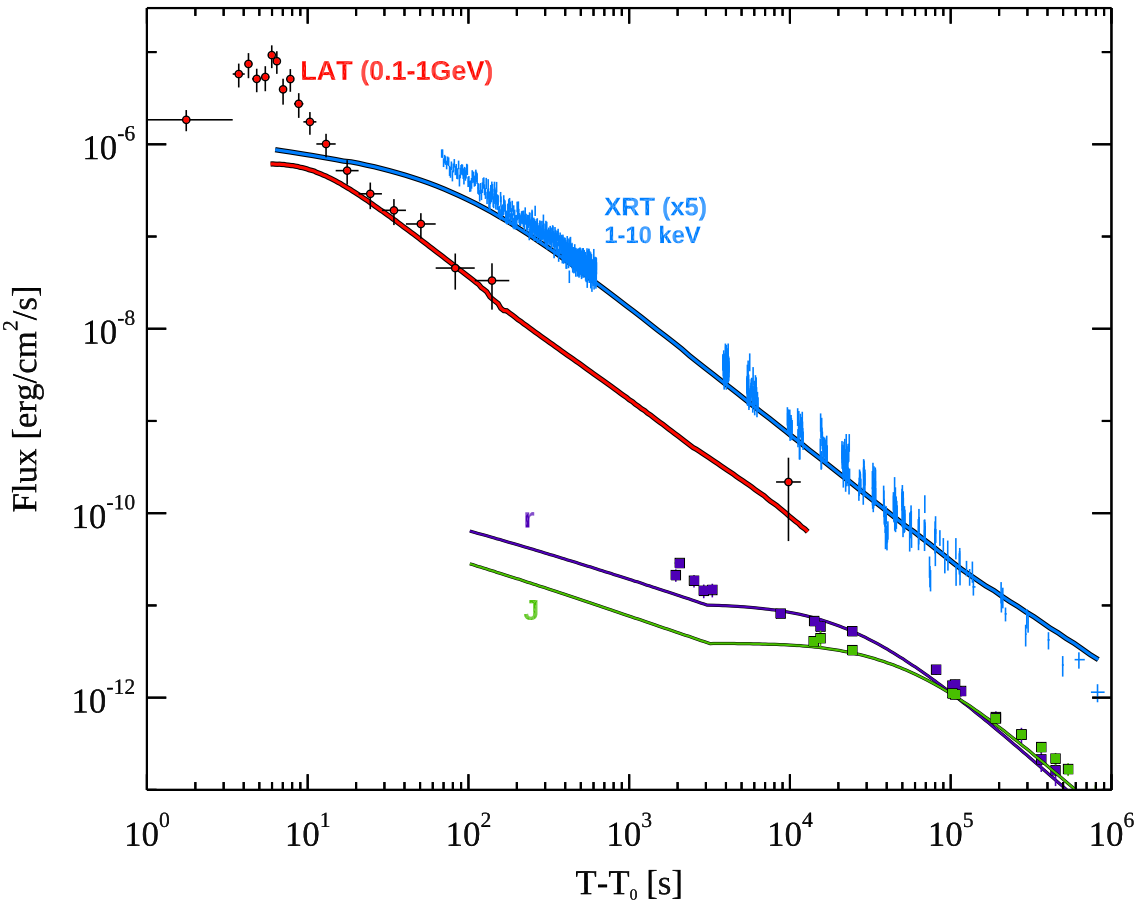

Extended Data Figure 12: **Modeling of X-ray, GeV and optical light curves.** Modeling of forward shock emission (solid curves) is compared to observations, at different frequencies. Red: 0.1-10 GeV; blue: 1-10 keV (the flux is multiplied by 5); purple: optical r band; green: near-infrared J filter. The first change in decay rate in optical-NIR lightcurves ($t \sim 3 \times 10^3$ s) is caused by the transition from the fast to the slow cooling regime. The second change in decay rate ($t \sim 8 \times 10^4$ s) is produced by the passage of $\nu_{\rm m}$ across the optical band, as shown in Fig. 11. At $t < 2 \times 10^3$ s, the reverse shock component is contributing to the optical flux[19].

10^5 s), the observed temporal decay requires a very steep value of $p > 3$ for $s = 0$ and a value between $p = 2.4$ and $p = 2.5$ for $s = 2$. The late time optical light curve is then more consistent with the temporal decay expected in case of a wind-like medium.

Summarizing, observations of X-ray and optical emission and their evolution in time support a wind-like medium ($s = 2$), with $p = 2.4 - 2.5$, where the emission is initially in fast cooling regime and transitions to a slow cooling regime around 3×10^3 s. $\nu_{\rm m}$ crosses the optical band at $t \sim 8 \times 10^4$ s, explaining the steepening of the optical light curve and the flattening of the optical spectrum. The optical spectral index at late times is predicted to be $(1-p)/2 \sim -0.72$, in agreement with observations. Modeling of the optical light curve (r filter) is shown in Extended Data Fig. 12. The passage of $\nu_{\rm m}$ across the optical band explains the temporal steepening and the temporal decays before and after the break. This is also supported by early time observations: independently of the density profile of the external medium and on the cooling regime of the electrons, one expects $\nu_{\rm m} \propto t^{-3/2}$, that places $\nu_{\rm m}$ in the X-ray band at 10^2 s:

$$\nu_{\rm m}(t = 8 \times 10^4\,) = 3 \times 10^{18}\,{\rm Hz} \left(\frac{t}{100\,{\rm s}}\right)^{-1.5} = 10^{14}\,{\rm Hz}\,. \quad (1)$$

The SED at $\sim$100 s is indeed characterised by a peak in between 5-30 keV (Fig. 3), that we interpret as the characteristic synchrotron frequency $\nu_{\rm m}$.

The X-ray band initially lies above (or close to) $\nu_{\rm m}$, and the break frequency $\nu_{\rm c}$ starts crossing the X-ray band around $2 - 4 \times 10^4$ s, producing the steepening in the decay rate (the cooling frequency increases with time for $s = 2$). In this case, before the temporal break, the decay rate is related to the spectral index of the electron energy distribution by $\alpha_{\rm X,1} = (2 - 3p)/4 \sim -1.3$,

for $p \sim 2.4 - 2.5$. Well after the break, this value of p predicts a decay rate $\alpha_{\rm X,1} = (1-3p)/4 = -1.55 - 1.62$. These numbers are consistent with the indices inferred from modeling the XRT light curve with a broken power law function. Overall, this interpretation is also consistent with the fact that the late time ($t > 10^5$ s) X-ray and optical light curves display similar temporal decays (Fig.1), as they lie in the same part of the synchrotron spectrum ($\nu_{\rm m} < \nu_{\rm opt} < \nu_{\rm X} < \nu_{\rm c}$).

An alternative possibility is that $\nu_{\rm c} \gg \nu_{\rm m}$ at all times, implying that the emission is always produced in a slow cooling regime. In this case, however, no break is predicted in the X-ray light curve and the value of p necessary to account for the temporal decay rate of XRT ($\alpha_{\rm X} \sim -1.36$ in case the light curve is modeled with a single PL) is harder, $p = 2.1 - 2.2$. This scenario is slightly disfavored, because it does not provide an explanation for the X-ray temporal break and predicts a late time temporal decay of the optical light curve that is shallower than observed.

Radio and sub-mm observations: The self-absorption synchrotron frequency $\nu_{\rm sa}$ is constrained to be between the radio and optical band at early times (10^4 s), evolving to lower frequencies at later times ($\nu_{\rm sa} \propto t^{-3/5}$) and eventually crossing the radio band. Observations at 1 GHz show indeed that $\nu_{\rm sa} \sim 1$ GHz at 10^5 s (Extended Data Fig. 11). This implies that at early times the radio flux should increase as $F_{\rm radio} \propto t^1$, consistently with observations (Extended Data Fig. 10). Late time radio/sub-mm light curves provide further strong evidence in favour of a wind-shaped external environment: the flux is constant in time (Extended Data Fig. 10), as expected in the slow cooling regime, between $\nu_{\rm sa}$ and $\nu_{\rm m}$.

MAGIC emission: the modeling is built with reference to the MAGIC flux and spectral indices

derived considering statistical errors only (see Extended Data Table 1 and green data points in Extended Data Fig. 2).

We focus first on the time intervals 68-110 and 110-180 s, during which the emission was simultaneously observed by XRT, BAT, GBM, LAT and MAGIC, providing simultaneous information on the synchrotron spectrum. The two 1 keV-1 TeV SEDs are shown in Fig. 3. In the first one (upper panel), LAT observations provide strong evidence for the presence of two separated spectral peaks. We test a scenario where the low-energy component (dominating the X-ray band) is synchrotron radiation and the second component (dominating in the MAGIC energy range) is SSC radiation from the same electron population accelerated at the forward shock.

A simple case where the bulk of the emission is produced in the Thomson scattering regime can be easily ruled out. In the Thomson regime, the ratio between the SSC and synchrotron peak energies provides a robust estimate of the minimum electron Lorentz factor $\gamma_{\rm m}$. Consistently with the information inferred from the modeling of the optical and X-ray emission, we assume here a regime of fast cooling, as inferred from the study of emission at lower frequencies (see previous sub-sections). However, we note that the same conclusions are valid in case of slow cooling. With reference to the 68-110 s time interval and considering $E^{\rm syn}_{\rm peak} \sim 10\,{\rm keV}$ and $E^{\rm ssc}_{\rm peak} \sim 100\,{\rm GeV}$ (see upper panel in Fig. 3) we derive:

$$\frac{\nu^{\rm SSC}_{\rm peak}}{\nu^{\rm syn}_{\rm peak}} \simeq 2\,\gamma_{\rm m}^2 \sim 10^7\,, \qquad \gamma_{\rm m} \sim 2\times 10^3 \tag{2}$$

For this small value of $\gamma_{\rm m}$, the initial assumption of the KN regime affecting the spectrum only

above the peak energy is satisfied:

$$\Gamma_{\rm KN}(\nu_{\rm m}) = \frac{m_{\rm e}\, c^2\, \Gamma}{h\nu_{\rm m}\,(1+z)} \tag{3}$$

and $\Gamma_{\rm KN} \sim 5 \times 10^3\, \Gamma_{2.2} > \gamma_{\rm m}$ (for $h\nu_{\rm m} \sim E^{\rm syn}_{\rm peak} \sim 10\,{\rm keV}$ and $\Gamma_{2.2} = \Gamma/10^{2.2}$). The small inferred value of $\gamma_{\rm m}$ has two implications: i) if the bulk Lorentz factor Γ is larger than 150 (that is a necessary condition to avoid strong γ-γ opacity, see below), a small $\gamma_{\rm m}$ translates into a small efficiency of the electron acceleration, with $\epsilon_{\rm e} < 0.05$, ii) the synchrotron peak energy can be located at $E^{\rm syn}_{\rm peak} \sim 10\,{\rm keV}$ only for $B\,\Gamma \gtrsim 10^5\,{\rm G}$. The term $B\,\Gamma$ is proportional to $\sqrt{\epsilon_{\rm B}\, A_\star}$. To explain the SSC flux, $\epsilon_{\rm B}$ can not be larger than $\epsilon_{\rm e}$, leading to a constraint on the density: $A_\star \gg 10$. This large value of the density is inconsistent with the requirement of $\Gamma > 150$, as the required amount of kinetic energy would be very large $E_{\rm k} > 10^{55}\,{\rm erg}$. A simple case of synchrotron and SSC radiation in the Thomson regime is then ruled out, implying that KN effects and/or internal opacity must play an important role [105,106].

We now consider the case $\Gamma_{\rm KN} < \gamma_m$. The SSC peak in this case should be located at:

$$h\nu^{\rm SSC}_{\rm peak} \simeq 2\,\gamma_{\rm m}\,\Gamma\, m_{\rm e}\, c^2/(1+z) \tag{4}$$

Imposing $E^{\rm ssc}_{\rm peak} \lesssim 100\,{\rm GeV}$ to explain the MAGIC photon index, implies $\gamma_{\rm m}\Gamma \simeq 10^5$. Again, for $\Gamma > 150$, the inferred value of the electron energy is $\gamma_{\rm m} \lesssim 10^3$, that leads to the same difficulties as before.

These calculations show that γ-γ opacity must play an important role in shaping the observed peak energy of the SSC spectrum. Relaxing the assumption that the intrinsic peak energy of the SSC is below 100 GeV, we can now consider larger values for $\gamma_{\rm m}$. From equation 3 it is evident

that for values $\gamma_{\rm m} > 5 \times 10^3$, $\Gamma_{\rm KN} < \gamma_{\rm m}$, and KN effects are also relevant.

We include KN effects[28] on the synchrotron and SSC spectral shape and attenuation of the high-energy radiation caused by internal γ-γ opacity. For a gamma-ray photon with energy E_γ, we estimate the opacity as:

$$\tau_{\gamma\gamma}(E_\gamma) = \sigma_{\gamma\gamma}\,(R/\Gamma)\,n_{\rm t}(E_\gamma)\,, \tag{5}$$

where $n_{\rm t} = L_{\rm t}/(4\,\pi\,R^2\,c\,\Gamma\,E_{\rm t})$ is the density of target photons in the comoving frame, $L_{\rm t}$ is the luminosity and $E_{\rm t} = (m_{\rm e}\,c^2)^2\,\Gamma^2/E_\gamma/(1+z)^2$ is the energy of target photons in the observer frame. Target photons for photons with energy $E_\gamma = 0.2 - 1\,$TeV and for $\Gamma \sim 120 - 150$ have energies in the range $4 - 30\,$keV. We now allow for SSC peak energies $E^{\rm SSC}_{\rm peak} > 100\,$GeV and investigate conditions for reproducing the observed SEDs and their temporal evolution (Fig. 2). The MAGIC photon index (Extended Data Table 1) and its evolution with time constrains in any case the SSC peak energy to be not much higher than 1 TeV: in general the internal opacity decreases with time and KN effects become less relevant. A possible softening of the spectrum with time, as the one suggested by the observations, requires that the spectral peak decreases with time and crosses the MAGIC energy range. As the SSC spectrum is very broad around the peak, KN and/or opacity still need to play a role also at late times ($\sim 2000\,$s) in order to explain soft photon indices $\Gamma_{\rm TeV} < -2$ (Extended Data Table 1). In the slow cooling regime, the SSC peak evolves to higher frequencies for a wind-like medium and decreases very slowly ($\nu^{\rm SSC}_{\rm peak} \propto t^{-1/4}$) for a constant-density medium (both in KN and Thomson regimes). A fast cooling regime is then favored, given the faster evolution of the peak energy to lower frequencies ($\nu^{\rm SSC}_{\rm peak} \propto t^{-1/2} - t^{-9/4}$ depending on medium and regime). A fast cooling regime is also favored by the late time optical observations,

that place $\nu_{\rm m}$ in the X-ray band at early times (see Eq. 1).

The conditions on the location of the SSC peak constrain the electron energy to be around $\gamma_{\rm m} \sim 4 - 8 \times 10^4$ at 100 s. We find that after including these effects, the observations can be satisfactorily reproduced. The results of the modeling are shown in Fig. 3. We stress that a more detailed analysis should also take into account the effect of pair production on the observed spectrum: a flat component from secondary emission from the pairs produced by the internal $\gamma - \gamma$ annihilation might indeed contribute to the LAT flux at early times. A good modeling of the observations is obtained for a bulk Lorentz factor around $120 - 140$. For the density of the external medium, we obtain a lower limit $A_\star > 1$, that also translates into a lower limit on the kinetic energy $E_{\rm k} > 2 \times 10^{53}$ erg. The relatively large density is in agreement with late time observations at ~ 1 GHz, that locate the self-absorption frequency. The estimate of the kinetic energy implies that at least half of the total initial explosion energy has not been radiated during the prompt phase and powers the afterglow phase. With these parameters, and using the constraints on the afterglow onset time ($t^{\rm aft}_{\rm peak} \sim 5 - 10$ s from the smooth component detected during the prompt emission) the initial bulk Lorentz factor is constrained to assume values in the range $\Gamma_0 \sim 300 - 600$.

The results of the broad band modeling is shown in Fig.3, and Extended Data Figs. 11 and 12 where model curves are overlaid to observations. The model curves shown in these figures have been derived using the following parameters: $\epsilon_{\rm e} = 0.06$, $\epsilon_{\rm B} = 6 \times 10^{-4}$, $\xi_{\rm e} = 0.11$, $p = 2.4$, $A_\star = 0.2$, and $E_{\rm k} = 8 \times 10^{53}$ erg.

1. Mészáros, P. Theories of Gamma-Ray Bursts. ARA&A **40**, 137–169 (2002). astro-ph/0111170.

2. Piran, T. The physics of gamma-ray bursts. *Reviews of Modern Physics* **76**, 1143–1210 (2004). astro-ph/0405503.

3. Gehrels, N., Ramirez-Ruiz, E. & Fox, D. B. Gamma-Ray Bursts in the Swift Era. ARA&A **47**, 567–617 (2009). 0909.1531.

4. Gehrels, N. & Mészáros, P. Gamma-Ray Bursts. *Science* **337**, 932 (2012). 1208.6522.

5. Kumar, P. & Zhang, B. The physics of gamma-ray bursts & relativistic jets. Phys. Rep. **561**, 1–109 (2015). 1410.0679.

6. MAGIC-Collaboration. Teraelectronvolt emission from a gamma-ray burst. *Nature* (2019).

7. Klebesadel, R. W., Strong, I. B. & Olson, R. A. Observations of Gamma-Ray Bursts of Cosmic Origin. ApJ **182**, L85 (1973).

8. Costa, E. *et al.* Discovery of an X-ray afterglow associated with the γ-ray burst of 28 February 1997. Nature **387**, 783–785 (1997). astro-ph/9706065.

9. Nava, L. High-energy emission from gamma-ray bursts. *International Journal of Modern Physics D* **27**, 1842003 (2018). 1804.01524.

10. The Milagro Collaboration: R. Atkins *et al.* Evidence for TeV Emission from GRB 970417a. *arXiv e-prints* astro–ph/0001111 (2000). astro-ph/0001111.

11. van Paradijs, J., Kouveliotou, C. & Wijers, R. A. M. J. Gamma-Ray Burst Afterglows. ARA&A **38**, 379–425 (2000).

12. Sari, R., Piran, T. & Narayan, R. Spectra and Light Curves of Gamma-Ray Burst Afterglows. ApJ **497**, L17–L20 (1998). astro-ph/9712005.

13. Granot, J. & Sari, R. The Shape of Spectral Breaks in Gamma-Ray Burst Afterglows. ApJ **568**, 820–829 (2002). astro-ph/0108027.

14. Meszaros, P. & Rees, M. J. Delayed GEV Emission from Cosmological Gamma-Ray Bursts - Impact of a Relativistic Wind on External Matter. MNRAS **269**, L41 (1994). astro-ph/9404056.

15. Ackermann, M. *et al.* Multiwavelength Observations of GRB 110731A: GeV Emission from Onset to Afterglow. ApJ **763**, 71 (2013). 1212.0973.

16. Mirzoyan, R. First time detection of a GRB at sub-TeV energies; MAGIC detects the GRB 190114C. *The Astronomer's Telegram* **12390** (2019).

17. Fermi & collaboration, S. GRB190114C. *journal* (2019).

18. Ravasio, M. E. *et al.* GRB 190114C: from prompt to afterglow? *arXiv e-prints* (2019). 1902.01861.

19. Laskar, T. *et al.* ALMA Detection of a Linearly Polarized Reverse Shock in GRB 190114C. *arXiv e-prints* (2019). 1904.07261.

20. Sari, R. & Esin, A. A. On the Synchrotron Self-Compton Emission from Relativistic Shocks and Its Implications for Gamma-Ray Burst Afterglows. ApJ **548**, 787–799 (2001). astro-ph/0005253.

21. Vietri, M. GeV Photons from Ultrahigh Energy Cosmic Rays Accelerated in Gamma Ray Bursts. *Physical Review Letters* **78**, 4328–4331 (1997). astro-ph/9705061.

22. Zhang, B. & Mészáros, P. High-Energy Spectral Components in Gamma-Ray Burst Afterglows. ApJ **559**, 110–122 (2001). astro-ph/0103229.

23. Razzaque, S. A Leptonic-Hadronic Model for the Afterglow of Gamma-ray Burst 090510. ApJ **724**, L109–L112 (2010). 1004.3330.

24. Mészáros, P., Razzaque, S. & Zhang, B. GeV-TeV emission from γ-ray bursts. New A Rev. **48**, 445–451 (2004).

25. Gupta, N. & Zhang, B. Prompt emission of high-energy photons from gamma ray bursts. MNRAS **380**, 78–92 (2007). 0704.1329.

26. Fan, Y.-Z. & Piran, T. High-energy γ-ray emission from gamma-ray bursts — before GLAST. *Frontiers of Physics in China* **3**, 306–330 (2008). 0805.2221.

27. Galli, A. & Piro, L. Prospects for detection of very high-energy emission from GRB in the context of the external shock model. A&A **489**, 1073–1077 (2008). 0805.2884.

28. Nakar, E., Ando, S. & Sari, R. Klein-Nishina Effects on Optically Thin Synchrotron and Synchrotron Self-Compton Spectrum. ApJ **703**, 675–691 (2009). 0903.2557.

29. Xue, R. R. *et al.* Very High Energy γ-Ray Afterglow Emission of Nearby Gamma-Ray Bursts. ApJ **703**, 60–67 (2009). 0907.4014.

30. Piran, T. & Nakar, E. On the External Shock Synchrotron Model for Gamma-ray Bursts' GeV Emission. ApJ **718**, L63–L67 (2010). 1003.5919.

31. Hamburg, R. GRB 190114C: Fermi GBM detection. *GRB Coordinates Network, Circular Service, No. 23707, #1 (2019/January-0)* **23707** (2019).

32. Kocevski, D. *et al.* GRB 190114C: Fermi-LAT detection. *GRB Coordinates Network* **23709**, 1 (2019).

33. Gropp, J. D. GRB 190114C: Swift detection of a very bright burst with a bright optical counterpart. *GRB Coordinates Network, Circular Service, No. 23688, #1 (2019/January-0)* **23688** (2019).

34. Ursi, A. *et al.* GRB 190114C: AGILE/MCAL detection. *GRB Coordinates Network* **23712**, 1 (2019).

35. Frederiks, D. *et al.* Konus-Wind observation of GRB 190114C. *GRB Coordinates Network* **23737**, 1 (2019).

36. Minaev, P. & Pozanenko, A. GRB 190114C: SPI-ACS/INTEGRAL extended emission detection. *GRB Coordinates Network* **23714**, 1 (2019).

37. Xiao, S. *et al.* GRB 190114C:Insight-HXMT/HE detection. *GRB Coordinates Network* **23716**, 1 (2019).

38. Selsing, J. GRB 190114C: NOT optical counterpart and redshift. *GRB Coordinates Network, Circular Service, No. 23695, #1 (2019/January-0)* **23695** (2019).

39. Castro-Tirado, A. GRB 190114C: refined redshift by the 10.4m GTC. *GRB Coordinates Network, Circular Service, No. 23708, #1 (2019/January-0)* **23708** (2019).

40. Ajello, M. *et al.* A Decade of Gamma-Ray Bursts Observed by Fermi-LAT: The Second GRB Catalog. ApJ **878**, 52 (2019). 1906.11403.

41. Tavani, M. *et al.* The AGILE Mission. *Astron. Astrophys.* **502**, 995–1013 (2009).

42. Meegan, C. *et al.* The Fermi Gamma-ray Burst Monitor. ApJ **702**, 791–804 (2009). 0908.0450.

43. Narayana Bhat, P. *et al.* The Third Fermi GBM Gamma-Ray Burst Catalog: The First Six Years. ApJS **223**, 28 (2016). 1603.07612.

44. Goldstein, A. *et al.* The Fermi GBM Gamma-Ray Burst Spectral Catalog: The First Two Years. ApJS **199**, 19 (2012). 1201.2981.

45. Barthelmy, S. D. *et al.* The Burst Alert Telescope (BAT) on the SWIFT Midex Mission. Space Sci. Rev. **120**, 143–164 (2005). astro-ph/0507410.

46. Krimm, H. A. *et al.* GRB 190114C: Swift-BAT refined analysis. *GRB Coordinates Network, Circular Service, No. 23724, #1 (2019)* **23724** (2019).

47. Atwood, A. A., W. B.Abdo *et al.* The Large Area Telescope on the Fermi Gamma-Ray Space Telescope Mission. ApJ **697**, 1071–1102 (2009). 0902.1089.

48. Kocevski, D. *et al.* GRB 190114C: Fermi-LAT detection. *GRB Coordinates Network* **23709**, 1 (2019).

49. Aleksić, J. *et al.* The major upgrade of the MAGIC telescopes, Part I: The hardware improvements and the commissioning of the system. *Astroparticle Physics* **72**, 61–75 (2016). 1409.6073.

50. Aleksić, J. *et al.* The major upgrade of the MAGIC telescopes, Part II: A performance study using observations of the Crab Nebula. *Astroparticle Physics* **72**, 76–94 (2016). 1409.5594.

51. Ahnen, M. L. *et al.* Performance of the MAGIC telescopes under moonlight. *Astroparticle Physics* **94**, 29–41 (2017). 1704.00906.

52. Domínguez, A. *et al.* Extragalactic background light inferred from AEGIS galaxy-SED-type fractions. MNRAS **410**, 2556–2578 (2011). 1007.1459.

53. Franceschini, A., Rodighiero, G. & Vaccari, M. Extragalactic optical-infrared background radiation, its time evolution and the cosmic photon-photon opacity. A&A **487**, 837–852 (2008). 0805.1841.

54. Finke, J. D., Razzaque, S. & Dermer, C. D. Modeling the Extragalactic Background Light from Stars and Dust. ApJ **712**, 238–249 (2010). 0905.1115.

55. Gilmore, R. C., Somerville, R. S., Primack, J. R. & Domínguez, A. Semi-analytic modelling of the extragalactic background light and consequences for extragalactic gamma-ray spectra. MNRAS **422**, 3189–3207 (2012). 1104.0671.

1154 56. Evans, P. A. *et al.* Methods and results of an automatic analysis of a complete sample of
1155 Swift-XRT observations of GRBs. MNRAS **397**, 1177–1201 (2009). 0812.3662.

1156 57. Greiner, J. *et al.* GROND—a 7-Channel Imager. *Publications of the Astronomical Society of*
1157 *the Pacific* **120**, 405 (2008). 0801.4801.

1158 58. Tody, D. IRAF in the Nineties. In Hanisch, R. J., Brissenden, R. J. V. & Barnes, J. (eds.)
1159 *Astronomical Data Analysis Software and Systems II*, vol. 52 of *Astronomical Society of the*
1160 *Pacific Conference Series*, 173 (1993).

1161 59. Krühler, T. *et al.* The 2175 Å Dust Feature in a Gamma-Ray Burst Afterglow at Redshift
1162 2.45. ApJ **685**, 376–383 (2008). 0805.2824.

1163 60. Bolmer, J. *et al.* Dust reddening and extinction curves toward gamma-ray bursts at $z > 4$.
1164 A&A **609**, A62 (2018). 1709.06867.

1165 61. Castro-Tirado, A. J. *et al.* A very sensitive all-sky CCD camera for continuous recording of
1166 the night sky. In Proc. SPIE, vol. 7019 of *Society of Photo-Optical Instrumentation Engineers*
1167 *(SPIE) Conference Series*, 70191V (2008).

1168 62. Gropp, J. D. *et al.* GRB 190114C: Swift detection of a very bright burst with a bright optical
1169 counterpart. *GRB Coordinates Network* **23688**, 1 (2019).

1170 63. Cepa, J. *et al.* OSIRIS tunable imager and spectrograph. In Iye, M. & Moorwood, A. F. (eds.)
1171 *Optical and IR Telescope Instrumentation and Detectors*, vol. 4008 of Proc. SPIE, 623–631
1172 (2000).

64. de Ugarte Postigo, A. *et al.* The distribution of equivalent widths in long GRB afterglow spectra. A&A **548**, A11 (2012). 1209.0891.

65. Steele, I. A. *et al.* The Liverpool Telescope: performance and first results. In Oschmann, J. M., Jr. (ed.) *Ground-based Telescopes*, vol. 5489 of Proc. SPIE, 679–692 (2004).

66. Chambers, K. C. *et al.* The Pan-STARRS1 Surveys. *arXiv e-prints* (2016). 1612.05560.

67. Tarenghi, M. & Wilson, R. N. The ESO NTT (New Technology Telescope): The first active optics telescope. In Roddier, F. J. (ed.) *Active telescope systems*, vol. 1114 of *Society of Photo-Optical Instrumentation Engineers (SPIE) Conference Series*, 302–313 (1989).

68. Smartt, S. J. *et al.* PESSTO: survey description and products from the first data release by the Public ESO Spectroscopic Survey of Transient Objects. A&A **579**, A40 (2015). 1411.0299.

69. Covino, S. *et al.* REM: a fully robotic telescope for GRB observations. In Moorwood, A. F. M. & Iye, M. (eds.) *Ground-based Instrumentation for Astronomy*, vol. 5492 of *Society of Photo-Optical Instrumentation Engineers (SPIE) Conference Series*, 1613–1622 (2004).

70. Roming, P. W. A. *et al.* The Swift Ultra-Violet/Optical Telescope. Space Sci. Rev. **120**, 95–142 (2005). astro-ph/0507413.

71. Siegel, M. H. & Gropp, J. D. GRB 190114C: Swift/UVOT Detection. *GRB Coordinates Network* **23725**, 1 (2019).

1191 72. Poole, T. S. *et al.* Photometric calibration of the Swift ultraviolet/optical telescope. MNRAS
1192 **383**, 627–645 (2008). 0708.2259.

1193 73. Breeveld, A. A. *et al.* An Updated Ultraviolet Calibration for the Swift/UVOT. In *American*
1194 *Institute of Physics Conference Series*, vol. 1358, 373–376 (2011). 1102.4717.

1195 74. Kuin, N. P. M. *et al.* Calibration of the Swift-UVOT ultraviolet and visible grisms. MNRAS
1196 **449**, 2514–2538 (2015).

1197 75. Bianchi, L. *et al.* GALEX catalogs of UV sources: statistical properties and sample science
1198 applications: hot white dwarfs in the Milky Way. Ap&SS **335**, 161–169 (2011).

1199 76. Wright, E. L. *et al.* The Wide-field Infrared Survey Explorer (WISE): Mission Description
1200 and Initial On-orbit Performance. AJ **140**, 1868–1881 (2010). 1008.0031.

1201 77. Arnouts, S. *et al.* Measuring and modelling the redshift evolution of clustering: the Hubble
1202 Deep Field North. MNRAS **310**, 540–556 (1999). astro-ph/9902290.

1203 78. Ilbert, O. *et al.* Accurate photometric redshifts for the CFHT legacy survey calibrated using
1204 the VIMOS VLT deep survey. A&A **457**, 841–856 (2006). astro-ph/0603217.

1205 79. Covino, S. *et al.* Dust extinctions for an unbiased sample of gamma-ray burst afterglows.
1206 MNRAS **432**, 1231–1244 (2013). 1303.4743.

1207 80. Kann, D. A., Klose, S. & Zeh, A. Signatures of Extragalactic Dust in Pre-Swift GRB After-
1208 glows. ApJ **641**, 993–1009 (2006). astro-ph/0512575.

81. Zafar, T. *et al.* VLT/X-shooter GRBs: Individual extinction curves of star-forming regions. MNRAS **479**, 1542–1554 (2018). 1805.07016.

82. Schlafly, E. F. & Finkbeiner, D. P. Measuring Reddening with Sloan Digital Sky Survey Stellar Spectra and Recalibrating SFD. ApJ **737**, 103 (2011). 1012.4804.

83. McMullin, J. P., Waters, B., Schiebel, D., Young, W. & Golap, K. CASA Architecture and Applications. In Shaw, R. A., Hill, F. & Bell, D. J. (eds.) *Astronomical Data Analysis Software and Systems XVI*, vol. 376 of *Astronomical Society of the Pacific Conference Series*, 127 (2007).

84. Wilson, W. E. *et al.* The Australia Telescope Compact Array Broad-band Backend: description and first results. MNRAS **416**, 832–856 (2011). 1105.3532.

85. Partridge, B. *et al.* Absolute Calibration of the Radio Astronomy Flux Density Scale at 22 to 43 GHz Using Planck. ApJ **821**, 61 (2016). 1506.02892.

86. Sault, R. J., Teuben, P. J. & Wright, M. C. H. A Retrospective View of MIRIAD. In Shaw, R. A., Payne, H. E. & Hayes, J. J. E. (eds.) *Astronomical Data Analysis Software and Systems IV*, vol. 77 of *Astronomical Society of the Pacific Conference Series*, 433 (1995). astro-ph/0612759.

87. Swarup, G. *et al.* The Giant Metre-Wave Radio Telescope. *Current Science, Vol. 60, NO.2/JAN25, P. 95, 1991* **60**, 95 (1991).

88. Cherukuri, S. V. *et al.* GRB 190114C: GMRT detection at 1.26GHz. *GRB Coordinates Network* **23762** (2019).

89. Tremou, L. *et al.* GRB 190114C: MeerKAT radio observation. *GRB Coordinates Network, Circular Service, No. 23760, #1 (2019)* **23760** (2019).

90. Camilo, F. *et al.* Revival of the Magnetar PSR J1622-4950: Observations with MeerKAT, Parkes, XMM-Newton, Swift, Chandra, and NuSTAR. ApJ **856**, 180 (2018). 1804.01933.

91. Jonas, J. & MeerKAT Team. The MeerKAT Radio Telescope. In *Proceedings of MeerKAT Science: On the Pathway to the SKA. 25-27 May*, 1 (2016).

92. Fender, R. *et al.* ThunderKAT: The MeerKAT Large Survey Project for Image-Plane Radio Transients. *arXiv e-prints* arXiv:1711.04132 (2017). 1711.04132.

93. Offringa, A. R. AOFlagger: RFI Software (2010). 1010.017.

94. McMullin, J. P., Waters, B., Schiebel, D., Young, W. & Golap, K. CASA Architecture and Applications. In Shaw, R. A., Hill, F. & Bell, D. J. (eds.) *Astronomical Data Analysis Software and Systems XVI*, vol. 376 of *Astronomical Society of the Pacific Conference Series*, 127 (2007).

95. Tasse, C. *et al.* Faceting for direction-dependent spectral deconvolution. A&A **611** (2018).

96. Smirnov, O. M. & Tasse, C. Radio interferometric gain calibration as a complex optimization problem. MNRAS **449**, 2668–2684 (2015).

97. Mohan, N. & Rafferty, D. PyBDSF: Python Blob Detection and Source Finder (2015). 1502.007.

98. Holland, W. S. *et al.* SCUBA-2: the 10 000 pixel bolometer camera on the James Clerk Maxwell Telescope. MNRAS **430**, 2513–2533 (2013). 1301.3650.

99. Currie, M. J. *et al.* Starlink Software in 2013. In Manset, N. & Forshay, P. (eds.) *Astronomical Data Analysis Software and Systems XXIII*, vol. 485 of *Astronomical Society of the Pacific Conference Series*, 391 (2014).

100. Chapin, E. L. *et al.* SCUBA-2: iterative map-making with the Sub-Millimetre User Reduction Facility. MNRAS **430**, 2545–2573 (2013). 1301.3652.

101. Dempsey, J. T. *et al.* SCUBA-2: on-sky calibration using submillimetre standard sources. MNRAS **430**, 2534–2544 (2013). 1301.3773.

102. Smith, I. A., Perley, D. A. & Tanvir, N. R. GRB 190114C: JCMT SCUBA-2 sub-mm observations. *GRB Coordinates Network, Circular Service, No. 23823, #1 (2019)* **23823** (2019).

103. Bošnjak, Ž., Daigne, F. & Dubus, G. Prompt high-energy emission from gamma-ray bursts in the internal shock model. A&A **498**, 677–703 (2009). 0811.2956.

104. Panaitescu, A. & Kumar, P. Analytic Light Curves of Gamma-Ray Burst Afterglows: Homogeneous versus Wind External Media. ApJ **543**, 66–76 (2000). astro-ph/0003246.

105. Derishev, E. & Piran, T. The physical conditions of the afterglow implied by MAGIC's sub-TeV observations of GRB 190114C. *arXiv e-prints* arXiv:1905.08285 (2019). 1905.08285.

106. Wang, X.-Y., Liu, R.-Y., Zhang, H.-M., Xi, S.-Q. & Zhang, B. Synchrotron self-Compton emission from afterglow shocks as the origin of the sub-TeV emission in GRB 180720B and GRB 190114C. *arXiv e-prints* arXiv:1905.11312 (2019). 1905.11312.

Correspondence Correspondence and requests for materials should be addressed to Razmik Mirzoyan (email: razmik.mirzoyan@mpp.mpg.de) or MAGIC (email: magic@mpp.mpg.de).

Author Contributions The MAGIC telescope system was designed and constructed by the MAGIC Collaboration. Operation, data processing, calibration, Monte Carlo simulations of the detector, and of theoretical models, and data analyses were performed by the members of the MAGIC Collaboration, who also discussed and approved the scientific results. L. Nava coordinated the gathering of the data, developed the theoretical interpretation, and wrote the main section and the section on Afterglow Modeling. E. Moretti coordinated the analysis of the MAGIC data, wrote the relevant sections, and, together with F. Longo, coordinated the collaboration with the Fermi team. D. Miceli, Y. Suda and S. Fukami performed the analysis of the MAGIC data. S. Covino provided support with the analysis of the optical data and the writing of the corresponding sections. Z. Bosnjak performed calculations for the contribution from prompt emission to TeV radiation and wrote the corresponding section. S. Inoue, R. Mirzoyan, A. Stamerra and A. Biland contributed in structuring and editing the paper. All MAGIC collaborators contributed to the editing and comments to the final version of the manuscript.

S. Campana and M. G. Bernardini extracted the spectra and performed the spectral analysis of *Swift*/BAT and *Swift*/XRT data. N. P. M. Kuin derived the photometry for the *Swift*/UVOT event mode data, and the uv grism exposure. M. H. Siegel derived the image mode Swift UVOT photometry. A. de Ugarte Postigo was principal investigator of ALMA program 2018.1A.00020.T, triggered these observations and performed

photometry. S. Martin reduced the ALMA Band 6 data. C. C. Thöne, S. Schulze, D. A. Kann, and M. Michałowski participated in the ALMA DDT proposal preparation, observations, and scientific analysis of the data. D. A. Perley was principal investigator of ALMA program 2018.1.01410.T and triggered these observations, and was also principal investigator of the LT programme and the JCMT programme. A. M. Cockeram analyzed the ALMA Band 3 and LT data, and wrote the LT text. S. Schulze contributed to the development of the ALMA Band 3 observing programme. I. A. Smith triggered the JCMT programme, analyzed the data, and wrote the associated text. N. R. Tanvir contributed to the development of the JCMT programme. K. Misra was the principal investigator of the GMRT programme 35_018. S. V. Cherukuri and V. Jaiswal analyzed the data. L. Resmi contributed to the observation plan and data analysis. E.T., I.H. and R.D. have performed the MeerKAT data analysis. G. Anderson, A. Moin, S. Schulze and E. Troja were principal investigator of ATCA program CX424. G. Anderson, M. Wieringa and J. Stevens carried out the observations. G. Anderson, G. Bernardi, S. Klose, M. Marongiu, A. Moin, R. Ricci and M. Wieringa analysed these data. M. Bell, J. Miller-Jones and L. Piro participated to the ATCA proposal preparation and scientific analysis of the data. The ePESSTO project was delivered by the following who have contributed to managing, executing, reducing, analysing ESO/NTT data and provided comments to the manuscript: J. P. Anderson, N. Castro Segura, P. D'Avanzo, M. Gromadzki, C. Inserra, E. Kankare, K. Maguire, M. Nicholl, F. Ragosta, S. J. Smartt. A. Melandri and A. Rossi reduced and analyzed REM data and provided comments to the manuscript. J. Bolmer was responsible for observing the GRB with GROND as well as for the data reduction and calibration. J. Bolmer and J. Greiner contributed to the analysis of the data and writing of the text. E. Troja triggered the *NuSTAR* TOO observations performed under DDT program, L. Piro requested the XMM-Newton data carried out under DDT program and carried out the scientific analysis of XMM-Newton and *NuSTAR*. S. Lotti analyzed the *NuSTAR* data and wrote the associated text. A. Tiengo and G. Novara analysed the XMM-Newton data and wrote the associated

text. AJCT led the observing BOOTES and GTC programs. AC, CJPP, EFG, IMC, SBP and XYL analyzed the BOOTES data whereas AFV, MDCG, RSR, YDH and VVS analyzed the GTC data and interpreted them accordingly. N. Tanvir created the X-shooter and AlFOSC figures. J. Fynbo, J. Japelj performed the analysis of X-shooter and AlFOSC spectra. D. Xu, P. Jakobsson contributed to NOT programme and triggering. D. Malesani performed photometric analysis of NOT data.

Acknowledgements The MAGIC Collaboration would like to thank the Instituto de Astrofísica de Canarias for the excellent working conditions at the Observatorio del Roque de los Muchachos in La Palma. The financial support of the German BMBF and MPG, the Italian INFN and INAF, the Swiss National Fund SNF, the ERDF under the Spanish MINECO (FPA2017-87859-P, FPA2017-85668-P, FPA2017-82729-C6-2-R, FPA2017-82729-C6-6-R, FPA2017-82729-C6-5-R, AYA2015-71042-P, AYA2016-76012-C3-1-P, ESP2017-87055-C2-2-P, FPA201790566REDC), the Indian Department of Atomic Energy, the Japanese JSPS and MEXT, the Bulgarian Ministry of Education and Science, National RI Roadmap Project DO1-153/28.08.2018 and the Academy of Finland grant nr. 320045 is gratefully acknowledged. This work was also supported by the Spanish Centro de Excelencia "Severo Ochoa" SEV-2016-0588 and SEV-2015-0548, and Unidad de Excelencia "María de Maeztu" MDM-2014-0369, by the Croatian Science Foundation (HrZZ) Project IP-2016-06-9782 and the University of Rijeka Project 13.12.1.3.02, by the DFG Collaborative Research Centers SFB823/C4 and SFB876/C3, the Polish National Research Centre grant UMO-2016/22/M/ST9/00382 and by the Brazilian MCTIC, CNPq and FAPERJ. L. Nava acknowledges funding from the European Union's Horizon 2020 Research and Innovation programme under the Marie Skłodowska-Curie grant agreement n. 664931. This paper makes use of the following ALMA data: ADS/JAO.ALMA#2018.A.00020.T, ADS/JAO.ALMA#2018.1.01410.T. ALMA is a partnership of ESO (representing its member states), NSF (USA) and NINS (Japan), together with NRC (Canada), MOST and

ASIAA (Taiwan), and KASI (Republic of Korea), in cooperation with the Republic of Chile. The Joint ALMA Observatory is operated by ESO, AUI/NRAO and NAOJ. CT, AdUP, and DAK acknowledge support from the Spanish research project AYA2017-89384-P. C. Thoene and A. de Ugarte Postigo acknowledge support from funding associated to Ramón y Cajal fellowships (RyC-2012-09984 and RyC-2012-09975). D. A. Kann acknowledges support from funding associated to Juan de la Cierva Incorporación fellowships (IJCI-2015-26153). The James Clerk Maxwell Telescope is operated by the East Asian Observatory on behalf of The National Astronomical Observatory of Japan; Academia Sinica Institute of Astronomy and Astrophysics; the Korea Astronomy and Space Science Institute; Center for Astronomical Mega-Science (as well as the National Key R&D Program of China with No. 2017YFA0402700). Additional funding support is provided by the Science and Technology Facilities Council of the United Kingdom and participating universities in the United Kingdom and Canada. The JCMT data reported here were obtained under project M18BP040 (P.I. D. Perley). We thank Mark Rawlings, Kevin Silva, Sheona Urquart, and the JCMT staff for the prompt support of these observations. The Liverpool Telescope, located on the island of La Palma in the Spanish Observatorio del Roque de los Muchachos of the Instituto de Astrofisica de Canarias, is operated by Liverpool John Moores University with financial support from the UK Science and Technology Facilities Council. The Australia Telescope Compact Array is part of the Australia Telescope National Facility which is funded by the Australian Government for operation as a National Facility managed by CSIRO. GEA is the recipient of an Australian Research Council Discovery Early Career Researcher Award (project number DE180100346) and JCAM-J is the recipient of Australian Research Council Future Fellowship (project number FT140101082) funded by the Australian Government. Support for the German contribution to GBM was provided by the Bundesministerium für Bildung und Forschung (BMBF) via the Deutsches Zentrum für Luft und Raumfahrt (DLR) under grant number 50 QV 0301. The UAH coauthors gratefully acknowledge NASA funding from cooperative agreement NNM11AA01A. C.A.W.H., and C.M.H. gratefully acknowl-

edge NASA funding through the *Fermi*-GBM project.

The *Fermi* LAT Collaboration acknowledges generous ongoing support from a number of agencies and institutes that have supported both the development and the operation of the LAT as well as scientific data analysis. These include the National Aeronautics and Space Administration and the Department of Energy in the United States, the Commissariat à l'Energie Atomique and the Centre National de la Recherche Scientifique / Institut National de Physique Nucléaire et de Physique des Particules in France, the Agenzia Spaziale Italiana and the Istituto Nazionale di Fisica Nucleare in Italy, the Ministry of Education, Culture, Sports, Science and Technology (MEXT), High Energy Accelerator Research Organization (KEK) and Japan Aerospace Exploration Agency (JAXA) in Japan, and the K. A. Wallenberg Foundation, the Swedish Research Council and the Swedish National Space Board in Sweden.

Additional support for science analysis during the operations phase is gratefully acknowledged from the Istituto Nazionale di Astrofisica in Italy and the Centre National d'Études Spatiales in France. This work performed in part under DOE Contract DE-AC02-76SF00515.

Part of the funding for GROND (both hardware as well as personnel) was generously granted from the Leibniz-Prize to Prof. G. Hasinger (DFG grant HA 1850/28-1). Swift data were retrieved from the Swift archive at HEASARC/NASA-GSFC, and from the UK Swift Science Data Centre.

This work is based on observations obtained with XMM-Newton, an ESA science mission with instruments and contributions directly funded by ESA Member States and NASA.

This work is partially based on observations collected at the European Organisation for Astronomical Research in the Southern Hemisphere under ESO programme 199.D-0143. The work is partly based on observations made with the Gran Telescopio Canarias (GTC), installed in the Spanish Observatorio del Roque de los Muchachos of the Instituto de Astrofísica de Canarias, in the island of La Palma. This work is par-

tially based on observations made with the Nordic Optical Telescope (programme 58-502), operated by the Nordic Optical Telescope Scientific Association at the Observatorio del Roque de los Muchachos, La Palma, Spain, of the Instituto de Astrofísica de Canarias. This work is partially based on observations collected at the European Organisation for Astronomical Research in the Southern Hemisphere under ESO programme 102.D-0662. This work is partially based on observations collected through the ESO programme 199.D-0143 ePESSTO. M. Gromadzki is supported by the Polish NCN MAESTRO grant 2014/14/A/ST9/00121. M. Nicholl is supported by a Royal Astronomical Society Research Fellowship M. G. Bernardini, S. Campana, A. Melandri and P. D'Avanzo acknowledge ASI grant I/004/11/3. S. Campana thanks for support the implementing agreement ASI-INAF n.2017-14-H.0. S. J. Smartt acknowledges funding from STFC Grant Ref: ST/P000312/1. NPMK acknowledges support by the UK Space Agency under grant ST/P002323/1 and the UK Science and Technology Facilities Council under grant ST/N00811/1. L. Piro, S. Lotti acknowledge partial support from the agreement ASI-INAF n.2017-14-H.0. VAF acknowledges RFBR 18-29-21030 for support. AJCT acknowledges support from the Junta de Andalucía (Project P07-TIC-03094) and support from the Spanish Ministry Projects AYA2012-39727-C03-01 and 2015-71718R. KM acknowledges the support from Department of Science and Technology (DST), Govt. of India and Indo-US Science and Technology Forum (IUSSTF) for the WISTEMM fellowship and Dept. of Physics, UC Davis where a part of this work was carried out. M.J.M. acknowledges the support of the National Science Centre, Poland through the grant 2018/30/E/ST9/00208. VJ and RL acknowledges support from the grant EMR/2016/007127 from Dept. of Science and Technology, India. K. Maguire acknowledges support from H2020 through an ERC Starting Grant (758638). L. Izzo would like to acknowledge Massimo Della Valle for invaluable support in the operation of the telescope.

Competing Interests The authors declare that they have nocompeting financial interests.